Programming Kirigami Through Fibre Steering

Master Thesis

Sander Wildenborg

Delft University of Technology

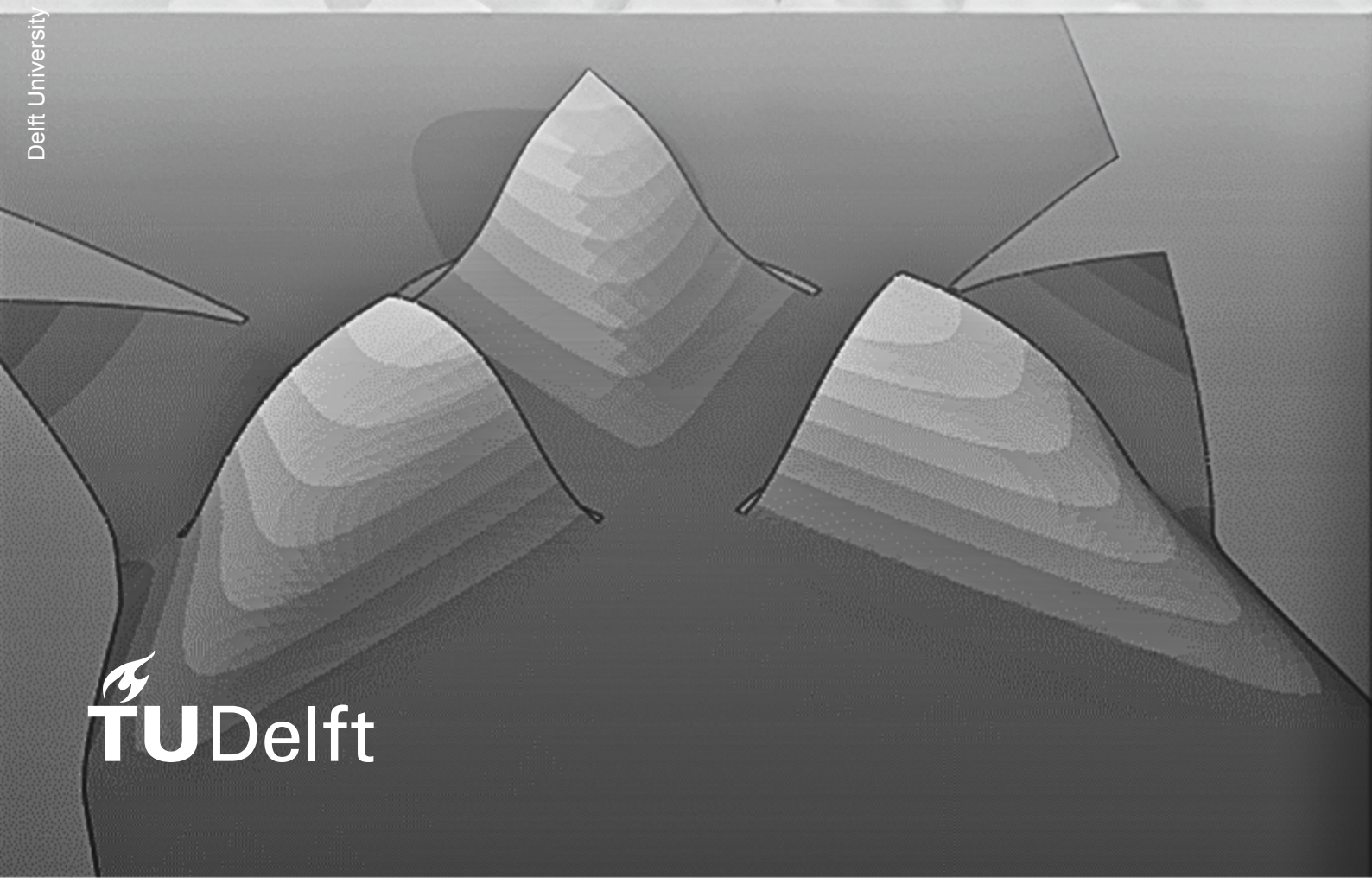

TU Delft

Programming Kirigami Through Fibre Steering

Master Thesis

Sander Wildenborg

to obtain the degree of Master of Science
at the Delft University of Technology,
to be defended publicly on Monday November 13, 2023 at 09:30 AM.

Student number: 4690362

Thesis committee:	Dr. K. Masania	TU Delft, supervisor
	Dr. C Dransfeld	TU Delft, chair
	Dr. I Balbin	TU Delft, examiner

An electronic version of this thesis is available at `https://repository.tudelft.nl/`.

Cover: Microscopy image showing denticles on the skin of a Leopard shark [1] (top). Finite element result of fibre steered kirigami (bottom).

TU Delft

Acknowledgments

This master thesis marks the end of my 7 year educational journey. After starting my bachelor in Mechanical Engineering, I soon started to develop a deep interest for aeronautics and space. After completion of my bachelor, I decided to pursue this passion and enroll myself for the Aerospace Engineering pre-master's program and consecutive master. Although this journey has been extensive I feel very proud to finally conclude it, and I am very grateful to everyone who helped me along the way.

First and foremost, I would like to express my deepest gratitude to my thesis supervisors Kunal Masania and Vinay Damodaran. Their expertise have pushed me to think further such that I gained a deeper understanding of my research results. I also very much value how they took the time to engage in in-depth, and sometimes very lengthy, discussions with me. The thoughtful feedback they provided has significantly improved the quality of this work. I would also like to say that they have a contagious enthusiasm for research. Their passion for exploring new and exciting knowledge has been truly inspiring. I will try to carry forward this enthusiasm into my future endeavours.

Secondly, I would like to thank the Shaping Matter Lab research group for the supportive and fun work environment that they created. Their feedback and the discussions we shared, whether during group meetings, in the hallways or in the lab has truly helped to shape this work. In particular, I would like to thank Caroline Houriet for her invaluable assistance with the GCODE generation.

Furthermore, I wish to express my gratitude to the DASML technicians (Pietro, Alexander, Chantal, Victor, Johan, Dave and Roy). I spent a considerable amount of time in the lab, their expertise and instructions have helped me during my sample manufacturing process and experiments.

My educational journey extended longer than this thesis, and I owe a debt of gratitude to those who helped me throughout. My family, my parents, my brothers and my girlfriend Kyra who always stood by me and assisted me along the way. I am deeply grateful for the unconditional love and support you have given me.

Sander Wildenborg
Amersfoort, October 2023

Abstract

Engineers and researchers are using natures complex system as inexhaustible source of inspiration to create new materials and structures which outperform conventional materials and structures. In particular shark skin has been extensively investigated for its mechanical- and biological protection and flow controlling capabilities. Shark skin consists of small scales called denticles which are optimized to the flow condition that is present at a specific location on the sharks body. With the optimized skin, sharks are able to swim faster by reducing drag. Efforts have been made to recreate such drag reducing capabilities on an airfoil by making use of kirigami structures which textured the surface. Results show that flow separation is delayed by making use of kirigami, however the results can be further optimized by locally changing out-of-plane deformation of the kirigami structure based on the flow conditions which are present at a specific location on the airfoil.

In this work, it is demonstrated that kirigami deformation behaviour can be controlled by tailoring the anisotropic material that is used to create the kirigami structure. The ultimate goal is to find a relationship between the material pattern and the deformation behaviour of the kirigami structure. A fused filament fabrication method was used to steer anisotropic thermoplastic polyurethane carbon fibre material in user defined orientations. By using this method, single layer kirigami samples were manufactured with a single cut. Five sample groups were manufactured, the main aim of the first three sample groups was to define a kirigami geometry which is most sensitive to material orientation change. Once these geometrical parameters were found, the unidirectional (UD) material orientation was varied in the fourth sample group and different symmetric orientation fields were used in the last sample group.

Each tested sample corresponded to a finite element (FE) model in Abaqus/CAE with identical geometry and material orientation. Results show that the FE model is able to capture the effect of a change in material orientation on the deformation behaviour of the kirigami structure. The FE model is validated by comparing the simulated kirigami tip deflection with actual test data. In order to show that the buckled shapes themselves compare rather well, a comparison study is done by overlaying both the tested surface and the surface that is a result from the FE simulation. The relative difference between the simulated- and experimental out-of-plane displacements did not exceed 13.7%.

A kirigami structure will invert a global uniaxial stretch into a local compression of the kirigami leaf. Therefore, the kirigami leaf can essentially be seen as a thin plate that follows classical plate buckling theory. By following this theory, two rules can be posed that can be used to estimate the shape of the fibre steered kirigami. The first rule states that a sheet with clamped sides will buckle in the shape of a smooth, symmetric, parabola when subjected to compression. The second rule states that the local slope of the buckled parabola is directly proportional to the bending stiffness of the structure. As the fibre steered kirigami exhibits variable stiffness, the slope of the parabola will change based on local material orientation. Two different buckled shapes will follow when both rules are applied, which shape is most dominant in the actual kirigami is dependent on the actual clamping conditions. As the clamping conditions are posed by the material in the hinge area, the local stiffness of the material will determine the strength of the boundary condition and thus the sensitivity of the structure to follow the material orientation. All simulated and tested buckled kirigami shapes followed the rules that have been posed.

Contents

Nomenclature

Abbreviations

Abbreviation	Definition
AM	Additive Manufacturing
CAD	Computer Aided Design
CF	Carbon Fibre
(3D)-DIC	(Three-Dimensional) Digital Image Correlation
FDM	Fused Deposition Modeling
FE	Finite Element
FFF	Fused Filament Fabrication
ISO	International Organization for Standardization
PLA	Polylactic Acid
STL	Stereolithography
TPE	Thermoplastic Elastomer
TPU	Thermoplastic Polyurethane
UD	Unidirectional

Symbols

Symbol	Definition	Unit
a	Width of kirigami unit cell	$[mm]$
b	Height of kirigami unit cell	$[mm]$
c	Distance between slit and clamp edge	$[mm]$
CL	Clamp length	$[mm]$
D	Displacement	$[mm]$
E_1	Elastic modulus along print direction	$[MPa]$
E_2	Elastic modulus perpendicular to print direction	$[MPa]$
G_{12}	In-plane shear modulus	$[MPa]$
G_{13}	Transverse shear modulus (along print direction)	$[MPa]$
G_{23}	Transverse shear modulus (perpendicular to print direction)	$[MPa]$
L	Characteristic length of kirigami unit cell	$[mm]$
l_c	Cut length	$[mm]$
N	Number of repeating unit cells	$[-]$
SW	Slit width	$[mm]$
t	Specimen thickness	$[mm]$
x	Hinge width	$[mm]$
γ	Cut angle	$[°]$
δ	Hinge length	$[mm]$
θ	Material orientation	$[°]$
ν_{12}	Poisson ratio (loaded along print direction)	$[-]$
ν_{21}	Poisson ratio (loaded perpendicular to print direction)	$[-]$

List of Figures

List of Tables

1 Introduction

1.1. Background

Present-day technological development requires lighter and stronger materials that perform beyond the limit of current artificial materials. In order to reach this, scientists and engineers are revisiting natures complex but efficient system to shape new materials and structures with multi-functional capabilities [2]. Sharks are a prime example of this. The evolution of sharks date back over about 400 million years in which their skin developed certain features giving the shark mechanical- and biological protection against bacteria and preventing other organisms from attaching and growing. Furthermore, some sharks even developed clever flow control mechanisms in order to gain higher swimming speeds by reducing drag [3] [4]. Shark skin consists of microscopic scales called denticles, which are equipped with riblets that are oriented along the flow direction. The denticles with accompanying riblets exhibit different geometries based on the location on the body of the shark and accompanying flow conditions. One of the drag reducing mechanisms is related to delaying flow separation. Separation of the flow occurs when the boundary layer stops following the contour of a surface in a wake. This induces turbulence in the flow which increases pressure drag. By delaying the separation point drag can be reduced. The part of the shark that is most prone to flow separation is at maximum girth (near the sharks gill), as the static pressure is lowest. Here, the shark skin denticles are hypothesized to trap the flow and reversing its direction, thereby delaying flow separation [5]. The drag reducing capabilities of shark skin can potentially be used as inspiration to decrease aircraft drag.

As aircraft drag is directly related to fuel consumption, engineers are in a constant quest to find innovative ways to decrease the drag. Aviation is responsible for 2.5% of global carbon dioxide emissions. As air traffic is expected to increase in the coming years, greenhouse gas emissions are expected to increase as well [6]. A potential new drag reducing device can make use of the flow separation delaying mechanism as seen in shark skin. The Japanese Art of Paper Cutting, also known as Kirigami could be used to create such a drag reducing device.

Kirigami is not as widely known as its Japanese counterpart Origami in which paper is folded in order to create complex three dimensional structures. Rather, in Kirigami paper is cut in specific patterns and will deform in specific shapes when the sheet is uniaxially stretched. By cutting, one is essentially releasing constraints from the system, thereby the structure can be subjected to much larger strains than normally could be expected from the material. There are many different cutting patterns, each related to its own specific deformation behaviour. Especially Kirigami types which exhibit out-of-plane deformation when stretched are of interest, as this behaviour is the main driver for the drag reducing mechanism as seen in shark skin. The advantage of using Kirigami is its actuation compared to other drag reducing devices. In Kirigami, multiple surfaces move out-of-plane by only stretching the material. Moving traditional flow controlling devices often require much more cumbersome, and therefore heavy, actuating systems thereby reducing the overall drag reduction effectiveness.

A Kirigami structure has been successfully implemented to act as a drag reducing device on an airfoil [7]. The authors used a repeating pattern with straight cuts, this pattern ensured out-of-plane deformation of the created sheet ligaments upon stretching. The Kirigami sheet was attached to the surface of the wing in different stretched states and with that different out-of-plane displacements which textured the wing surface. The wing was placed in an airflow whereby the angle of attack was varied. Results show that the Kirigami in its most stretched state, had the largest flow separation delaying effect. The authors highlight that their setup could be optimized by (locally) varying the degree of texturing on the wing surface by using a different Kirigami cut pattern. This effect is, as discussed, also seen in sharks. The denticle geometry of the sharks skin changes based on location and accompanying flow conditions on the shark.

A potential new approach to control Kirigami deformation behaviour is by steering the anisotropic (fibre reinforced) material that is used to make the structure. By doing so, an extra parameter to design a Kirigami structure is essentially added. One is able to program the deformation behaviour of such structures either globally or locally by varying the material pattern. Hereby, shark inspired skins can be manufactured that vary geometry and accompanying deformation behaviour throughout the structure. The main aim of this thesis is to manufacture, test and simulate fibre steered Kirigami and to ultimately find a relationship between the used fibre pattern and deformation behaviour of such structures.

1.2. Outline

This thesis starts with a brief exploration of the current state-of-the-art regarding Kirigami and ways to manufacture and ultimately control its deformation behaviour. In chapter 3 a gap in literature will be defined which ultimately leads to the research questions and scope of this work. The method to manufacture, test and simulate the fibre steered Kirigami structures will be explained in chapter 4. In chapter 5 five different fibre steered Kirigami samples are manufactured. The main aim of the first three sample groups is to validate the test setup and define the Kirigami geometry which is most sensitive to a change in material orientation. Once this geometry is defined, only the material orientation will be changed in the last two sample groups. Each tested sample corresponds to a digital model with the same geometry and material orientation. This deformation behaviour of this model is simulated by using a finite element method in Abaqus which is ultimately validated by comparing its output with actual test data. Based on the observations and analysis done during testing and simulation, a conclusion is formulated in chapter 6. The recommendations for future work can be found in chapter 7.

2

Literature Study

2.1. The Art of Paper Cutting

Kirigami surfaces are known for their peculiar and counter-intuitive mechanical behaviour such as super-stretchability, morphability, buckling and multistability. The concept of kirigami will be explained in this section.

2.1.1. Classification of kirigami surfaces

There are many different kirigami patterns, each pattern has their own specific deformation behaviour. In order to classify them, they can be categorized into two different groups: cut-only kirigami and cut-and-fold kirigami [8]. They can be further divided in: fractal-cut kirigami, ribbon kirigami, lattice kirigami, zigzag kirigami and closed-loop kirigami, as shown in figure 2.1. Cut-only kirigami surfaces can be directly produced using 3D-printing techniques by excluding material where the cuts should be made. Cut-and-fold kirigami need, as opposed to cut-only kirigami, an extra production step after 3D-printing in which the folding takes place. Because of this reason only fractal-cut kirigami and ribbon kirigami are explored in this section.

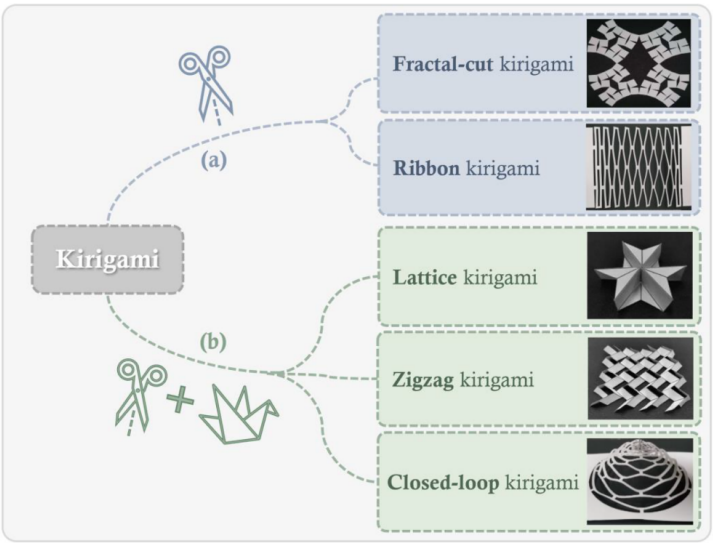

Figure 2.1: Classification of kirigami surface types [8].

Fractal-cut kirigami

Fractal-cut kirigami can be recognized by its mainly in-plane deformation when strained, therefore this kirigami type is also known as planar kirigami in literature. As shown in figure 2.2A fractal-cut kirigami is created by placing cuts in such a way that either square- or triangular units cells are formed [9].

When the structure is biaxially loaded the units remain rigid while the hinges that connect the units are strained, this allows the units to rotate with respect to each other. Fractal-cut kirigami surfaces are often made of a flexible material as the strain is very localized around the hinge points, stiff materials are generally not able to sustain these strains. When the kirigami structure reaches its fully stretched state, moment equilibrium is reached. However, the structure can be deformed even further, at this point the square- or triangular units will also start to strain. The total deformation in a fully stretched state can be increased by introducing so called hierarchical cuts. This means that the cut pattern is repeated and embedded within an existing unit cell. Figure 2.2B shows a silicone rubber sheet with no cuts (level 0), a repeated pattern of cuts (level 1), a repeated pattern of cuts with an embedded pattern (level 2) and a repeated pattern with two embedded patterns (level 3). Finite element analysis results show that increasing the amount of hierarchical levels in the repeating pattern increases the maximum lateral strain to 43%, 62% and 79% for hierarchical level 1, -level 2 and -level 3 respectively [9]. The total deformation of kirigami sheets can therefore be many times greater than otherwise could not be accomplished by the material itself [8].

The concept of using fractal-cuts to create kirigami surfaces has been used to create patterns with interesting mechanical behaviour. It was shown that kirigami surfaces with rectangular unit cells instead of square ones show an even higher stretchability [10]. Auxetic materials generally show anisotropic behaviour, but by applying either six-fold or three-fold symmetry in the cut pattern of the unit cell it was demonstrated that auxetic materials with an isotropic response could be created [11]. Some effort has also been put into reverse designing kirigami with an algorithm that takes the desired deformed shape and outputs a cutting pattern [12].

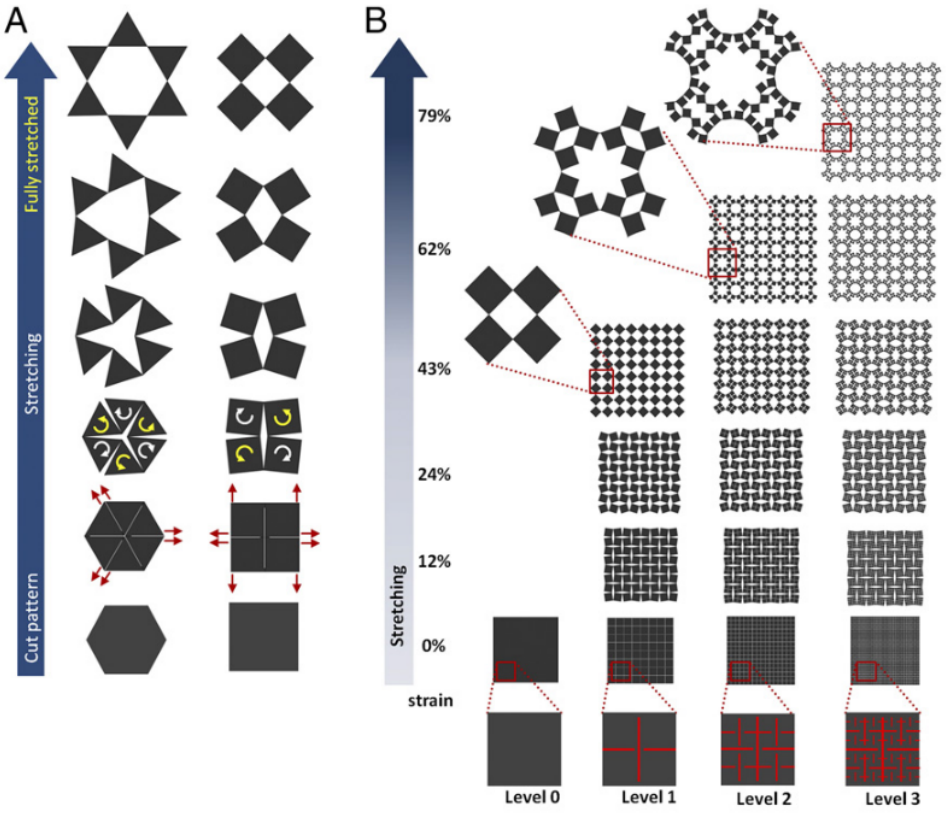

Figure 2.2: A: By perforating an elastic sheet with orthogonal cuts, either square- or triangular units cells can be created. The units cells will rotate with respect to each other when the structure is biaxially loaded. Thereby a much larger strain can be attained than the material is able to reach without the cuts. B: Hierarchical levels can be added to the cutting pattern by repeating and embedding the unit cell. This way the structure can be stretched even further. Adapted from: [9]

Ribbon kirigami
Ribbon kirigami can be recognized by the buckling behaviour when strained, therefore this kirigami type is also known as buckling-induced kirigami in literature [13]. Kirigami surfaces of this type generally move out-of-plane because of the local buckling of the ligaments when uniaxially loaded. These ligaments do not have a preferred buckling direction when the kirigami surface lacks imperfections. Imperfections can be purposely added to force the ligaments to buckle in a certain direction. This mechanism can be utilized to control the deformation behaviour of kirigami surfaces, and will futher explained in section 2.2.1. Generally, ribbon type kirigami structures have a more distributed strain over its ligaments as opposed to fractal-cut type kirigami structures where strain is concentrated in its hinges [14].

2.1.2. Mechanics of ribbon type kirigami surfaces

When a parallel-cut kirigami sheet is stretched, multiple regimes during deformation can be recognized [14], as can be seen in figure 2.3A and figure 2.3B. The reaction force in the sheet rises quickly in the initial regime as all ligaments only deform in-plane. The deformation in this stage is very similar to the deformation of the fractal-cut type kirigami which are known for their in-plane deformation behaviour. When the uniaxial strain is large enough, the ligaments start to rotate around their hinges and will move out-of-plane [8]. When the uniaxial strain is further increased, buckling eventually occurs, causing a drop in reaction force. This buckling behaviour is counter-intuitive as structures generally only buckle under a critical compression load, whereas kirigami ligaments will buckle under a global uniaxial stretch. This behaviour is driven by the kinematics imposed by the cut pattern, which will 'invert' global uniaxial stretch to localized compression of the ligaments [14]. When the uniaxial stretch is further increased beyond the buckling transition point the kirigami sheet enters the second regime. In this stage the sheet can be deformed significantly while the rise in reaction force is limited. The reaction force increases again in the final regime. In this stage deformation behaviour in the hinges changes from bending- to stretching dominated [13]. As a consequence, the reaction force increases rapidly again up to the point when the hinges start to tear and the kirigami structure eventually fails [8]. It must be noted that this deformation behaviour is not limited to parallel-cut kirigami but for all ribbon type kirigami surfaces in general.

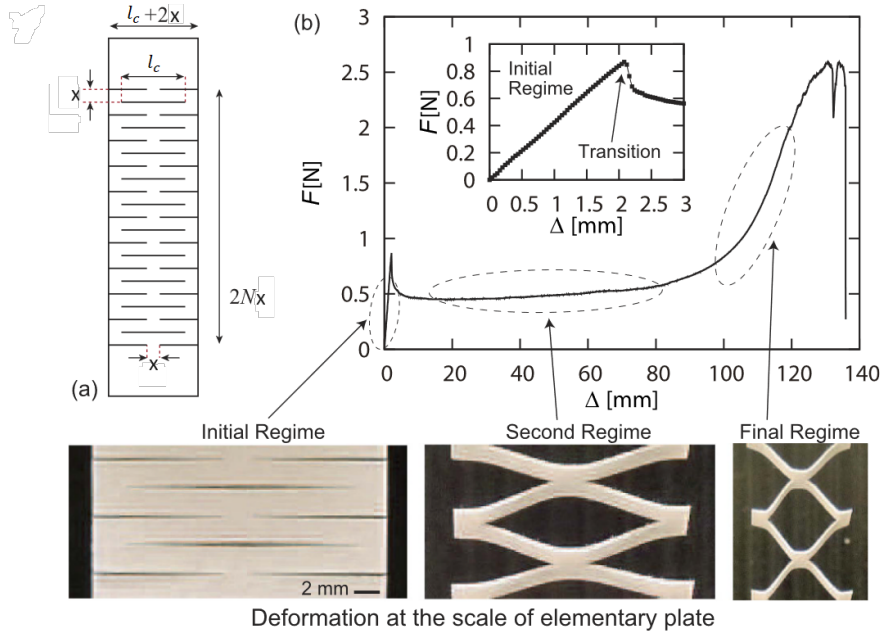

Figure 2.3: Deformation behaviour of a ribbon type kirigami sheet. Adapted from: [15]

The buckling transition that occurs between the initial regime and the second regime was studied in depth. It is theorized that the in-plane energy is competing with the out-of-plane energy in the ligaments and when the magnitude of both energies become equal buckling occurs [15]. An equation can be

formulated which relates geometric parameters of the kirigami structure to the critical uniaxial stretch at which buckling occurs. In order to arrive at such an equation the parallel-cut kirigami in figure 2.3A is considered. It is assumed that $l_c \approx l_c + 2x$ as $l_c \gg x$, $2N$ represents the total amount of segments in the kirigami structure, t is the sheet thickness and D represents the uniaxial stretch. When the thin plate theory for small deflections is used, the in-plane energy during the initial regime can be written as:

$$U_I(\Delta) \approx 2NEx^3tD_1^2/l_c^3, \ for\ D_1, x \ll l_c \tag{2.1}$$

here, D_1 is the in-plane deflection and equal to $\Delta/(2N)$. The out-of-plane energy during the second regime can be written as:

$$U_{II}(\Delta) \approx 2NEt^3xD_2^2/l_c^3, \ for\ D_2, x \ll l_c \tag{2.2}$$

here, D_2 is the out-of-plane deflection and $D_2^2 = (\Delta/2N + x)^2 - x^2$. Buckling occurs when both energies become equal. So by equating the two expressions above, the critical in-plane stretch (i.e. buckling stretch) can be written as follows [15]:

$$\Delta_c = 2ND_c, \ where\ D_c = \frac{2t^2x}{x^2 - t^2} \tag{2.3}$$

It can be seen that many parameters cancel out and only the geometric parameters of the kirigami structure remain.

A kirigami pattern can in essence be seen as a network of cracks in a plate. When the plate is thin enough, the cracks will cause local buckling in the structure before the cracks will propagate [16, 17]. This effect can be explained with figure 2.4. Here, a uniaxial tensile force is imposed on a thin rectangular plate with a crack with length l_c. The figure shows a mapping of the normalized sum of principal stresses over the surface. It can be seen that a local compression is inflicted around the crack, this compression will cause the plate to buckle when the plate is sufficiently thin. It must be noted than in kirigami structures with multiple cuts, adjacent unit cells will influence each other. This effect is known as the neighbour-neighbour effect, in which the buckled surface in a unit cell, influences the curving of material in the adjacent unit cell, thereby biasing its buckling behaviour [18].

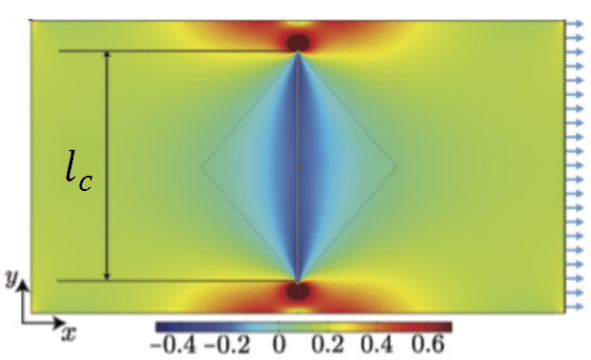

Figure 2.4: Normalized sum of principal stresses in a single cut sheet under uniaxial tension. Adapted from: [19]

Buckling of the kirigami ligaments is associated with a local minimum of internal energy. Most kirigami patterns display two local minima, each corresponding with their own stable structural state. Kirigami structures are able to switch between these stable states with snap-through behaviour [20]. This behaviour only occurs with an external force that directs the kirigami ligament to a different stable state until it eventually 'snaps' into place.

2.2. Controlling kirigami deformation behaviour

2.2.1. Passive control

The deformation behaviour of the kirigami surface can be altered by changing the geometric parameters of the structure. Mainly the sheet thickness and vertical- and horizontal distances between the slits influence the critical in-plane stretch [8]. The influence of changing vertical- and horizontal distances

and cut length of ribbon type kirigami has been investigated both numerically and experimentally [21]. Figure 2.5 shows both the experimental- and the FE results which are embedded within the graphs. The three deformation regimes that have been explained can be recognized. It can be seen that the critical buckling load increases when either the vertical- or the horizontal distance is increased. The amount of strain before failure also increases considerably when the vertical distance is increased. The kirigami structure is softened when the cut length is increased, meaning that the critical buckling load decreases and stretchability increases. In conclusion, the larger the hinges the higher the rigidity meaning that a higher critical buckling load is imparted, and increasing cutting length decreases rigidity.

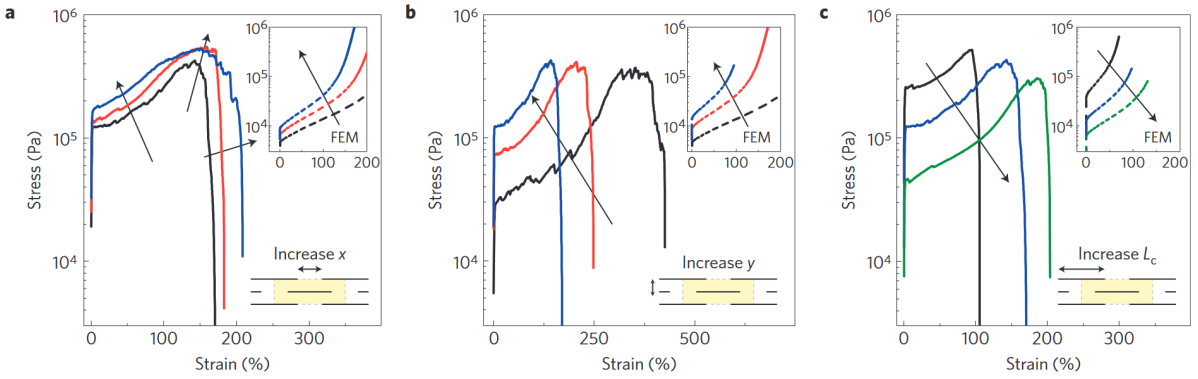

Figure 2.5: Change in kirigami deformation behaviour by changing geometric parameters [21].

By incorporating notches (local thinning) near the kirigami cuts the previously random buckling direction of ligaments can be prescribed in an explicit direction, this concept is known as kiri-kirigami in literature [18]. This concept can be seen in figure 2.6.

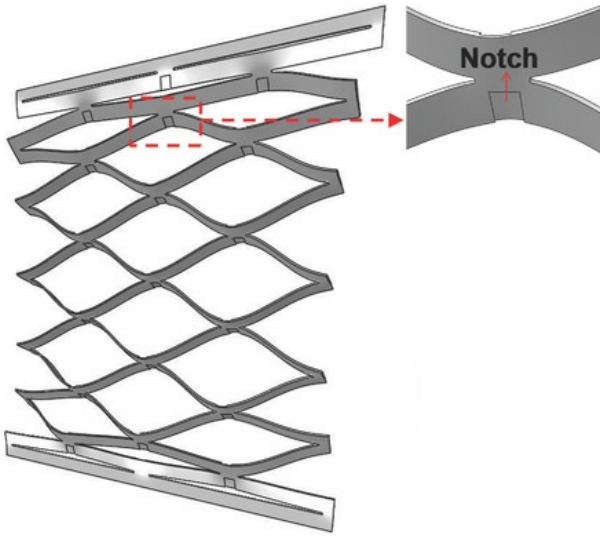

Figure 2.6: Controlling kirigami buckling direction by locally thinning the structure [18].

2.2.2. Active control

The approaches that have been discussed thus far are able to passively control kirigami deformation behaviour. There are two approaches that are able to alter deformation behaviour of kirigami structures after manufacturing by means of a mechanical stimulus.

The first approach to actively control kirigami deformation behaviour is by moving one of the fixtures that hold the kirigami surface in an out-of-plane direction. By doing so, one can force the kirigami ligaments to buckle in a certain direction [22].

The second approach to actively control kirigami deformation behaviour is by imposing curvature to the kirigami surface which is typically flat. By modifying the amount of curvature of the sheet, the 'popping' sequence of the kirigami ligaments can be changed [23]. Figure 2.7 shows how this concept works. By imposing curvature, the ligaments will start to pop sequentially rather than simultaneously. The research concluded that an increase curvature will result in a larger divergence between the ligaments located at the top- and bottom of the structure to fold. When applied in for instance soft robotics or wearables, the kirigami metasurface can change its deformation behaviour depending on the prevailing curvature.

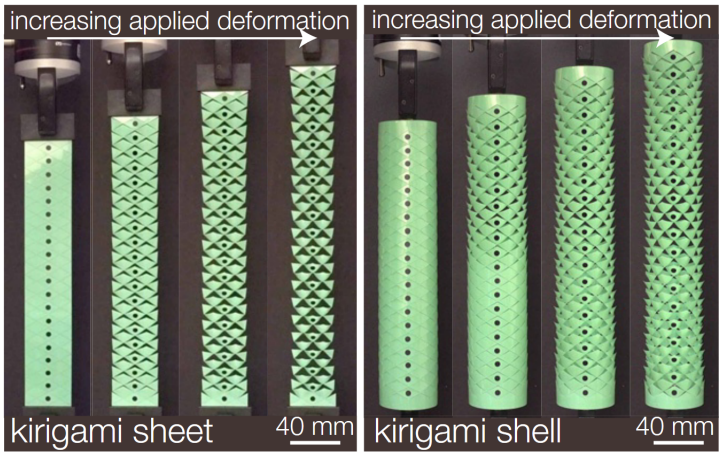

Figure 2.7: Sequential popping of kirigami ligaments by imposing curvature on the sheet [23].

2.3. 3D-printing kirigami surfaces

2.3.1. Fused Filament Fabrication

Fused filament fabrication (FFF) is an additive manufacturing technique in which material is deposited in a layer wise fashion. By stacking these layers successively, a part can be build. This technique is also known as fused deposition modelling in literature.

First of all, a computer aided design (CAD) model is created, this model is converted to a stereolithographic (STL) file which can be read by slicer software. The slicer software can be used to define many different printing parameters including nozzle temperature, bed temperature, infill density, infill pattern, layer thickness and many others. Once these parameters are set, the software will slice the digital part into different layers and generate a code that holds machine instructions, which is called GCODE [24]. FFF printers use thermoplastic polymers. By pushing the polymer filament through a heated nozzle, the filament will be heated above the melting temperature. Once this temperature is reached, the polymer chains are able to slide over each other and the material is able to flow. The importance of a proper nozzle design in this context must be noted, as the filament must reach a soft stage at the right place in the nozzle. When the filament is softened too soon, it cannot longer act as a piston that pushes the filament out of the nozzle [25]. Once the material properly exits the nozzle, it forms a bead which is fused to the part. This way, the part is build layer by layer, once a layer is completed, either the build platform or the extruder will move in z-direction, such that the next layer can be made, see figure 2.8. This process is repeated until the part is finished. The surface finish of a printed part is mainly determined by nozzle diameter, smaller nozzles will typically generate a smoother surface finish. However, a smaller nozzle size will limit the material flow, and therefore printing speed. The strength of a printed part is mainly determined by the bonding between each layer, which can be regulated by giving the print line sufficient heat energy such that polymer linkages can be formed, this way the layers will bond properly [26].

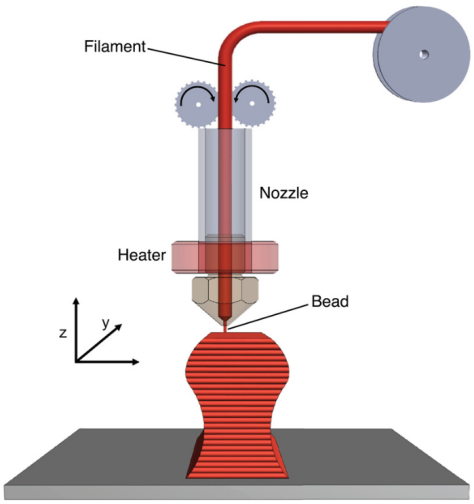

Figure 2.8: Fused filament fabrication 3D printing process [24].

The influence of printing orientation on the resulting mechanical properties has been looked into very extensively in literature. It is found that dog-bone specimen which are either printed on their edge or flat on the bed show higher tensile properties compared to specimen which are printed up-right [27–29]. The specimen which is printed up-right is loaded perpendicular to the print lines, thereby the load is not directed along the print lines (as is the case for the edge- or flat printed specimen) but is transferred between adjacent print lines, which is the weaker direction.

The effect of printing temperature on the mechanical properties of parts has been studied numerous of times as well. It is found that an increase in temperature results in an increase in adhesion strength of the printed lines, thereby the mechanical properties of the 3D-printed part tend to increase [30]. When printing at a higher temperature, the material is able to flow better (decrease in viscosity), one study showed that the amount of voids decreased because of this and therefore the fracture resistance of 3D-printed samples improved [31]. It must be noted that an increase in temperature only improves mechanical properties to a certain amount, when the temperature is set too high it may cause the polymer to (partially) decompose, which will affect the mechanical properties of the printed part in a negative manner [32].

Lastly, also the effect of layer height on mechanical properties of the 3D-printed part has been looked into. Researchers did not come up with a definite relationship however. Some studies found that the tensile properties reduce when the layer thickness is increased [33–38], and other studies observed at first a decrease of tensile properties but this was followed by an increase of properties when layer thickness was further increased [39, 40]. Some studies were not able to identify any relationship between layer thickness and tensile properties at all [41, 42].

Based on the parameters studied in this section it can be concluded that the printing parameter and mechanical properties relationship can for a large part be related to the adhesion strength of the print lines, this applies to both the adhesion of a printed line in a layer and between successive layers. The adhesion is generally weak, therefore 3D-printed parts are generally stronger when loaded along the direction of a print line and weaker in the direction with many successive print lines. Therefore, by changing printing parameters (e.g. build orientation, printing temperature and layer height) either the bond strength or the orientation of the bond can be changed and with that the (directional) mechanical properties of the part can be altered.

2.3.2. 3D-printing kirigami surfaces

Kirigami structures are generally produced with laser cutting which is a subtractive manufacturing technique. This method is able to produce precise and small cuts, however the intensity of the laser can cause the material properties to be altered locally. This can cause an unintentional bias in popping

direction. In contrast, 3D-printing enables full control over the properties in every part of the structure, which opens up possibilities to intentionally create features that influence the out-of-plane behaviour of the kirigami surface. Where section 2.3.1 has touched upon the general FFF technique, this section focuses more on the combination between kirigami and FFF.

Nakajima et al. [43] performed a study in which FFF has been used to manufacture kirigami surfaces, the effect of various printing parameters on the tensile properties of 3D-printed TPU kirigami samples was investigated. A parallel-cut kirigami pattern has been used, with in total 5 unit cells. Figure 2.9 shows the geometry of the kirigami samples, and table 2.1 summarizes the values of the dimensions that have been used. A slit height of 1 mm was the minimum value that was found for which the the slits did not stick together. The samples were printed with a print speed of 288 mm/min as the quality of the samples was the highest using this speed. In total 20 kirigami specimen were manufactured, 5 specimen for each of the following stacking sequences (infill direction): $[0/0]_4$, $[90/90]_4$, $[90/0]_4$ and $[45/-45]_4$. All other printing parameters were kept constant. The specimen were loaded in tension in an universal tensile testing machine with a 2 kN load cell. It was found that the $[0/0]_4$ and the $[90/0]_4$ specimen had the highest average tensile strength (at break) with a value of 2.16 MPa and 2.43 MPa respectively. The $[90/90]_4$ specimen had the lowest tensile strength (at break) with an average value of 1.81 MPa. This discrepancy in strength is in line with expectations, as has been explained in section 2.3.1. Hereby it must be noted that some regions in the $[0/0]_4$ specimen were purely loaded in transverse direction with respect to the print direction during the deformation cycle. This was not the case for the $[90/0]_4$ specimen, as these always have extrudates along the loading direction during deformation. The researchers also investigated the effect of specimen thickness on deformation behaviour, they used the specimen with the $[90/0]_n$ stacking sequence, as these samples gave the lowest standard deviation in the results for tensile strength (at break). In total 5 specimen were manufactured for each of the following thickness variations: 1 mm $([90/0]_2)$, 1.5 mm $([90/0]_3)$, 2 mm $([90/0]_4)$ and 2.5 $([90/0]_5)$ with a layer thickness of 0.25 mm. Results show that there is a large variation in elongation (at break) between the thinner samples (1 mm and 1.5 mm) and the thicker samples (2 mm and 2.5 mm). It is observed that the thicker samples are purely moving in-plane, and the thinner samples are moving both in- and out-of-plane. It is this change in deformation behaviour that causes a discrepancy in elongation (at break).

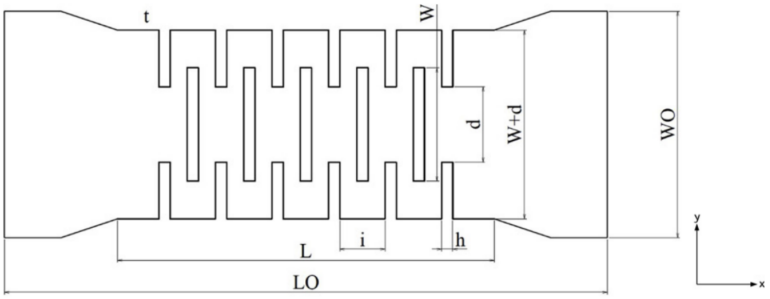

Figure 2.9: Geometry of 3D-printed TPU kirigami sample [43].

Table 2.1: Geometrical values of 3D-printed TPU kirigami sample [43]

Parameter	Description	Value (mm)
W	Slit Width	15
h	Slit Height	1
i	Slit Interval	5
d	Distance between slit ends	10
t	Specimen thickness	2
$W+d$	Width of kirigami	25
L	Length between grips	50
LO	Specimen length	80
WO	Width of the grip section	30

Amin [44] looked into using elastic materials to create angled cut kirigami, which is a ribbon type kirigami, through 3D-printing. Angled cut patterns show the highest out-of-plane stiffness, and can therefore be applied to surface texturing applications (e.g. in flow separation delay- or drag controlling devices in aircraft). The geometry of the angled cut pattern which has been used in this study can be seen in figure 2.10. The parameters of interest were the cut angle (γ) and the dimensionless parameter δ/L, which is the ratio between the hinge length parallel to the cut (δ) and the characteristic length (L). The actual geometrical values used to characterize the deformation behaviour of the kirigami structure are shown in table 2.2. A TPE material is used to create the kirigami surfaces, which is a mixture between a plastic and a rubber. This combination allows for thermoplastic processability while the material simultaneously exhibits rubber-like mechanical properties. Previous research suggested that the thinner the kirigami surface the larger the (out-of-plane) deformation. However, this research showed that thin samples created through 3D-printing showed warpage due to residual thermal stresses. Therefore, the samples were not made as thin as possible, but thin enough to show a profound deformation. Similar to the study performed by Nakajima et al. [43], Amin [44] reported slit fusion as well. In order to prevent slit fusion, a higher dimensional accuracy must be guaranteed. To do this, the following guidelines regarding manufacturing of the samples were posed:

- Multiple perimeters should be printed to prevent infill lines to expand beyond the outer geometry of the part.
- Outer perimeters should be printed first.
- A concentric infill pattern should be used, hereby the nozzle moves along the slits, thereby a higher accuracy of the slit shape is reached.
- A setting that compensates for the expansion/shrinkage of the material (known as XY size compensation) should be optimized.

After manufacturing, the samples were uniaxially loaded with a universal tensile testing machine, by using Digital Image Correlation (DIC) the displacements could be measured. The vertical displacement (stretching of the samples) and out-of-plane displacement were extracted from this data such that the out-of-plane strain and out-of-plane angular deflection of the ligaments could be calculated. It was found that the samples with smaller cut angles give a larger out-of-plane deflection angle and samples with a higher δ/L ratio show a slight increase in out-of-plane deflection. Hereby it was observed that the amount of uniaxial tensile force required to reach a certain out-of-plane deflection angle increases with an increase in the δ/L ratio. Another interesting observation is a bias in buckling direction. It was found that the kirigami ligaments had the tendency to buckle in the direction opposite of the print bed. A possible explanation for this bias is a slight increase in thickness towards the centre of the kirigami ligaments on the top surface. This thickness increase is caused by the concentric infill, hereby the nozzle 'pushes' the material towards the middle.

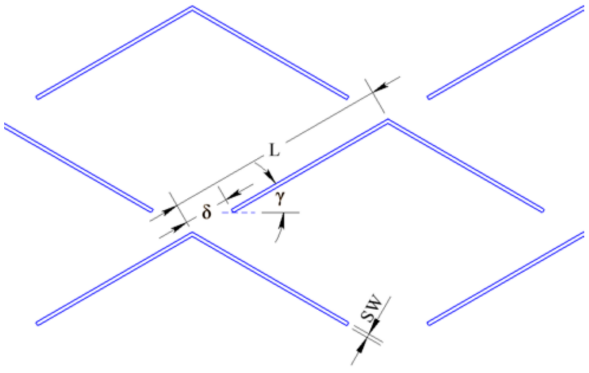

Figure 2.10: Characteristic geometric parameters of the angled cut pattern [44].

Table 2.2: Values of geometrical parameters in the angled cut pattern of 3D-printed TPE kirigami sample [44]

γ (°)	δ/L	Number of samples
20	0.10	4
30	0.10	4
30	0.15	4
30	0.20	4
40	0.10	4
50	0.10	4
60	0.10	4

As can be concluded from previous research, 3D-printing, like laser cutting can cause a bias in popping direction as well. However, 3D-printing enables a higher degree of control of the properties that drive this bias, compared to laser cutting. There are more parameters at play which can be tuned in order to either in- or decrease this tendency. Because 3D-printing enables a large control of the material properties in the printed structure, it can also be used to alter the deformation behaviour of the kirigami structure either locally or globally. A limitation that 3D-printing brings is warpage of the printed structure due to residual thermal stresses. This effect becomes more profound when the structure is thin, as is the case for kirigami surfaces. Therefore, the structure can not be too thin, but simultaneously needs to be thin enough such that it can properly deform under the imposed strains.

2.3.3. 3D-printing short fibre reinforced polymers

A considerable amount of research related to modeling and understanding extrusion and orientation behaviour has been conducted in the field of short fibre extrusion processes. It is shown that the flow field geometry of the melt has a significant effect on fibre orientation, the flow field geometry is defined by nozzle geometry and swell of the extruded material once it exits the nozzle [45, 46]. In particular swelling can be interesting as it can be controlled during the 3D-printing process. Bertevas et al. [47] performed a numerical study of the FFF printing process with fibre-reinforced polymers. In this study, a core-shell structure was observed, the shell exhibits fibres which are highly oriented in the print direction, the fibres are oriented to a lesser degree in the core. It is found that the core-shell structure becomes more evident in a flow field that exhibits swelling in front of the nozzle. This swelling arises when the velocity of nozzle is lower than the velocity of the material exiting the nozzle. The speed of the material that is exiting the nozzle is related to the flow rate of the material, layer height and layer width which are printing parameters.

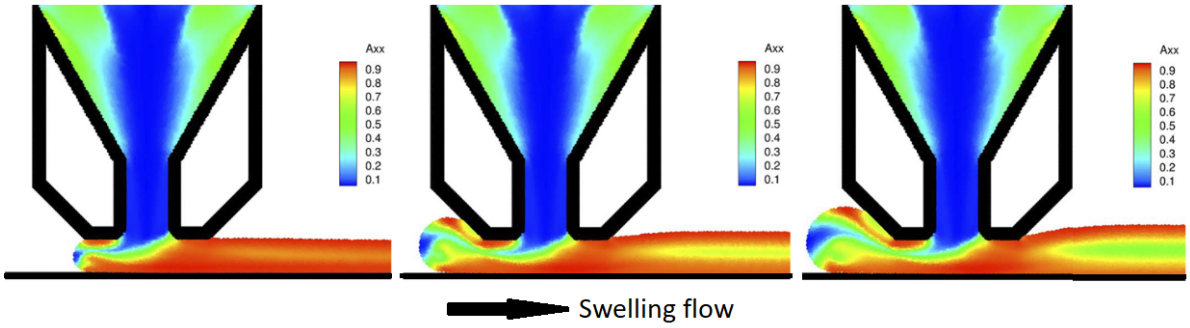

Figure 2.11: Modeling of short fibre orientation during FFF process, the presence of a core-shell structure in the printed line becomes more apparent when the flow is swelling in front of the nozzle. Adapted from: [47]

3

Research Definition

3.1. Research objective

As discussed in chapter 2, there are several ways to passively control kirigami surfaces. These mechanisms are driven by a change in geometry of the structure. Yet, the potential of the incorporation of anisotropy that could result from the fused filament fabrication process (FFF) remains unexplored. The FFF process enables full control over the material orientation and resulting variable stiffness in the structure and can therefore be used to create the fibre steered kirigami.

The main aim of this study is to find a relationship between the material orientation field of printed thermoplastic polyurethane reinforced with carbon fibres (TPU CF) and resulting behaviour change in the kirigami structure. By taking measurements of the buckled shape of the kirigami structure, one is able to asses the effects of a certain introduced material orientation. In order to drive future research, a finite element (FE) model will be developed which is able to accurately predict the buckled shape of a kirigami structure based on user defined material orientation input. This model will be validated by comparing its output with actual sample test data.

3.2. Research questions

Following the research objective, the main research question of this study can be formulated as follows: **How can the buckled shape of angled cut kirigami structures be controlled by exploiting the anisotropy that results from 3D-printed TPU CF material?** The main research question can be divided into two sub-questions:

1. What is the relationship between the printed fibre pattern and the buckled shape of the kirigami structure under uniaxial loading?
2. What are the characteristics of a validated finite element model that simulates the deformation of a kirigami structure with printed fibres?

3.3. Scope

In order to mitigate any unwanted biases in the buckled shape of the kirigami, two limitations regarding the kirigami structure are posed. First of all, the tested kirigami samples will have a single cut. This way the neighbour-neighbour effect as discussed in subsection 2.1.2 will be completely omitted from the result. Secondly, the samples will be 3D-printed with a single layer. This way the laminate coupling effects are kept to a minimum. These limitations will ensure that any behaviour change observed is only caused by the introduced material orientation. This work will first investigate the effect of the kirigami geometry (cut angle γ and hinge length δ) on the behaviour change resulting from the introduced material orientation. Once the values for cut angle and hinge width for which the behaviour change is most significant are found, the kirigami geometry is fixed and the effect of material orientation itself on the buckled shape will be looked into.

4

Methodology

4.1. Manufacturing

4.1.1. Materials and printing setup

Thermoplastic polyurethane with reinforcing carbon fibres (TPU CF filament) will be used to create the samples, the filament has a diameter of 1.75 mm. The properties of TPU are similar to that of rubber. Yet, TPU will melt under elevated temperatures, rather than decompose, which makes it compatible with the fused filament fabrication process. The addition of small carbon fibres gives the TPU (which is milky transparent) a dark black appearance. These carbon fibres align during printing, giving the resulting structure anisotropic properties. The filament is produced by Smart Materials 3D [48]. As the filament is hygroscopic, it is dried in a oven at 70 °C for 4 hours after unpacking, as recommended by the supplier. After this drying step, the filament was kept in an airtight box with silica gel which absorbs moisture from the air that is present in the container. To ensure that the moisture content in the filament is as low as possible, the filament is dried every 2 weeks, with the same settings as mentioned above.

The Prusa MK3S+ printer was used to manufacture the samples. A textured PEI powder-coated steel build plate was used. The textured bed aids the removal of printed products compared to smooth PEI beds. Thereby, the chance of damaging the printed samples will decrease during the removal process when using textured beds. As carbon fibres erode standard (brass) nozzles fairly quickly, the E3D V6 hardened steel nozzle with a size of 0.4 mm was used. The full setup can be seen in figure 4.1.

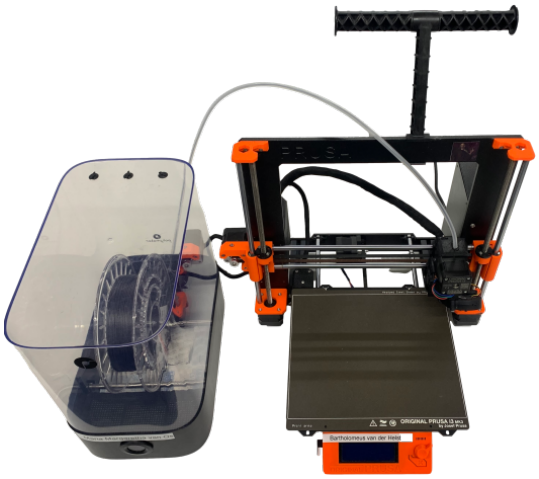

Figure 4.1: Printing setup: the Prusa MK3S+ printer was used to print the TPU CF material, which was stored in an airtight box with silica gel. The printer was equipped with a hardened steel nozzle and a textured build plate.

4.1.2. Kirigami geometry

In order to define the entire geometry of the kirigami structure using only a few parameters, a similar approach will be used as in the work of Amin [44]. Here, the geometry of angled cut kirigami is defined by the characteristic length of the periodic lattice L, hinge length δ, cut angle γ, slit width SW and sheet thickness t, as indicated by figure 2.10. The resulting geometry that results from these parameters can be patterned in vertical- and horizontal direction by defining the number of repeating unit cells in both directions. In the current work, the mechanical response of a kirigami structure with only one unit cell will be investigated such that the neighbour-neighbour effect is omitted. The kirigami structure, which can be seen in figure 4.2 can therefore be defined by the driving parameters L, δ, γ, SW and t. In order to ensure significant out-of-plane displacement, the loads have to be properly introduced into the samples. Therefore, extra clamp length CL is added on both sides of the kirigami structure. The dimensions of the unit cell (indicated with the dashed parallelogram) can be found by using the driving parameters and simple trigonometry. The following equations describe the width- (a) and height of the unit cell (b) respectively:

$$a = 2 \cdot L \cdot cos(\gamma) \tag{4.1}$$

$$b = 2 \cdot L \cdot sin(\gamma) \tag{4.2}$$

In order to ensure that the cut is centered between the clamps, the distance between the slit and the edge of the clamp (c) is described by the following equation:

$$c = \frac{SW}{cos(\gamma)} + b/2 \tag{4.3}$$

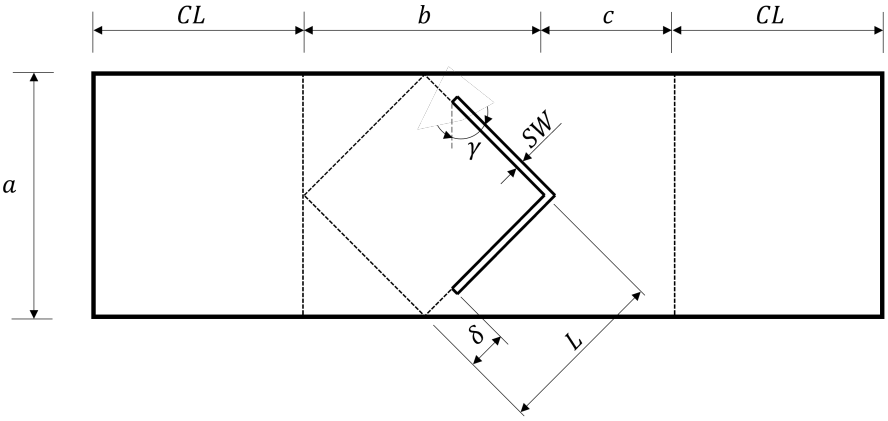

Figure 4.2: Geometric parameters of single unit cell kirigami samples. All dimensions are related to the driving parameters characteristic length L, hinge length δ, cut angle γ, slit width SW and sheet thickness t.

4.1.3. Generating GCODE

In order to 3D-print the kirigami samples, GCODE has to be generated. GCODE holds consecutive commands for the 3D-printer to perform. The most common method for generating GCODE is through the use of slicer software. However, this method imposes limitations on the current work, as user specified material directions need to be included. Therefore, larger control over tool paths is required then is available in conventional slicer software. Yet, the work by Houriet et al. [49] poses a solution. The authors created a MATLAB script which generates GCODE based on an user defined orientation field and bandwidth. The code creates streamlines based on the (material) angles defined in the orientation field, the coarseness of the streamlines is defined by the bandwidth, which essentially sets the spacing between the lines. By overlaying the plotted streamlines with a black and white masking image, lines are omitted where the respective image is black. Finally, GCODE by generated by converting the streamlines into machine tool paths and accompanying material extrusion. It turns out that this algorithm works very well for the kirigami application in this work. In order to make the GCODE generation process even smoother, more scripts are created.

The overview of the GCODE generation process can be seen in figure 4.3. First, the Abaqus model is initiated through a Python script and the kirigami model, with user defined material orientation, is created. At this point, the structure of the Abaqus model will not be further elaborated, as it is not of importance for the GCODE generation process. Subsection 4.4.1 will dive deeper in the architecture of the FE model. The most important takeaway is that two text files are generated upon initiation of the model. These files hold the geometric- and orientation data of the kirigami structure. The geometric data consists of the driving parameters of the kirigami structure (L, δ, γ, SW, t and CL), as all structural dimensions are related to these parameters. The orientation data consists of an m by n matrix in which every entry represents the angle of the material at a specific location in radians. As the MATLAB script overlays the masking image with the orientation field, entry θ_{11} represents the material angle at the top left corner of the kirigami structure. As discussed, the GCODE generation script requires a black and white image of the structure as an input. This image is generated with a different MATLAB script, an example of such an image can be seen in the figure. When the kirigami GCODE generation script is initiated, the black and white image (geometrical data) along with the geometry- and orientation text files will be automatically loaded. It will then overlay the structure with the orientation field and eventually generate the GCODE.

The decision to couple the Abaqus model with the GCODE generation process has been actively made. When not coupled, one needs to change parameters by hand in the MATLAB scripts, which gives room for errors. With this workflow, the user only has to initiate the Abaqus model, which will communicate its data to MATLAB through text files in order to create the GCODE. This way it is ensured that a printed kirigami sample has an accompanying FE model with identical geometrical features. This helps during validation of the Abaqus model, as data from this model will be compared to actual test data of the samples.

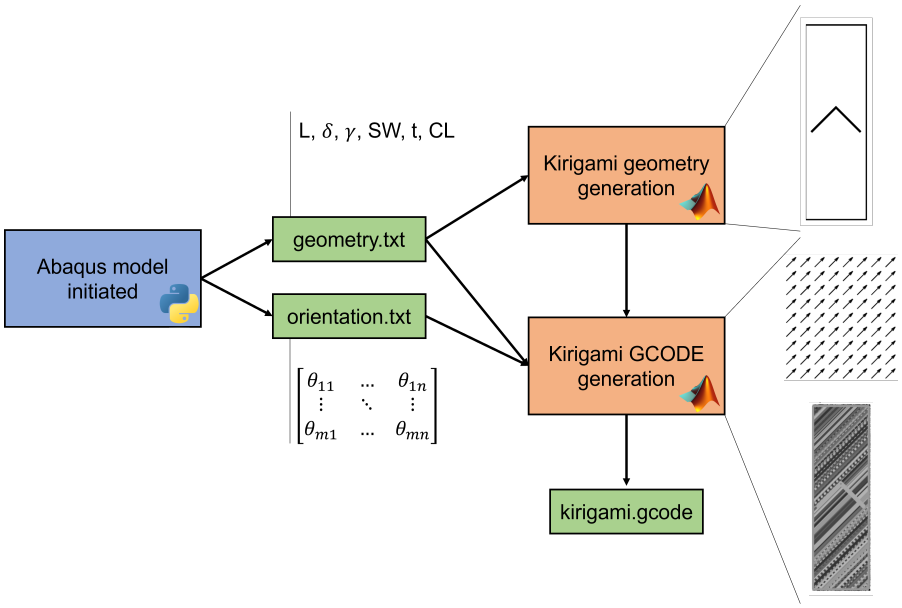

Figure 4.3: Overview of the GCODE generation process. First of all, the Abaqus model is initiated through Python, hereby two text files are generated which contain data about the geometry- and orientation of the kirigami structure. With this data, a black and white image of the geometry is generated. This image serves as input for the kirigami GCODE generation MATLAB script which will omit print lines at the locations at which the image is black, and generate print lines in the correct orientation at the locations at which the image is white.

4.1.4. Optimized print settings

Three main printing issues had to be solved before the TPU CF could be printed smoothly. The first issue that had to be overcome was nozzle clogging. A probable cause might have been fibre build up inside the nozzle and eventually blocking any flow out of the nozzle. An example of this issue can be seen in figure 4.4A, in which at first the printed lines only consisted of TPU (milky transparent color), after which full blockage occurs and the flow of material completely stops. This issue was eventually

resolved by optimizing both the printing temperature and the print speed. By optimizing these printing parameters, the pressure inside the nozzle was essentially optimized. With a optimized combination found, the TPU CF filament could be properly printed while still maintaining a high enough printing speed. The second issue was oozing of filament during travel movements. These are unwanted artefacts during a print process, as material should not be deposited while the nozzle travels over the printed lines. A typical example of this is displayed in figure 4.4B. The issue was resolved by optimizing both the retraction settings and Z-hop settings. Retraction refers to the movement of the extruder motor before the nozzle will make a travel motion. With the filament retraction set to zero, material will ooze out of the nozzle due to gravity. This can be prevented by optimizing these settings. Also the Z-hop height was optimized. This setting refers to the height of the nozzle during travel motions. Its value was chosen such that the nozzle opening would move slightly above the already printed lines (0.05 mm gap). This way the nozzle opening would be partially blocked by the printed lines, thereby minimizing oozing. A printed sample which required many travel motions can be seen in figure 4.4C, the travel motions can clearly be seen. Some of the nozzle travel motions passed over the slits, thereby fusing the slit partially together, as can be seen in figure 4.4D. Samples with a quality resembling the specimen in figures 4.4C and 4.4D were accepted, as filament oozing could not be solved completely. In order for the samples to move freely out-of-plane during testing, the partially fused slits were carefully cut open with a razor blade.

As highlighted in subsection 2.3.3, extruded material reinforced with fibres is known to swell to a diameter larger than the nozzle diameter. As the GCODE generating MATLAB script by Houriet et al. [49] assumed a non-swelling material, an extra printing parameter was therefore added in the script called 'Extrusion Multiplier' which accounted for this effect. This parameter, along with the 'live adjust Z' setting on the Prusa, were optimized. During this extrusion optimization, samples were printed in which either under-extrusion (as can be seen in figure 4.4E), or over-extrusion occurred. With optimized values found, specimen could be printed with a thickness equal to the layer height specified in the MATLAB script, and with all print lines properly fused together. The printing parameters that were found by overcoming the printing issues and used to create the samples for the buckled shape tests are listed in table 4.1.

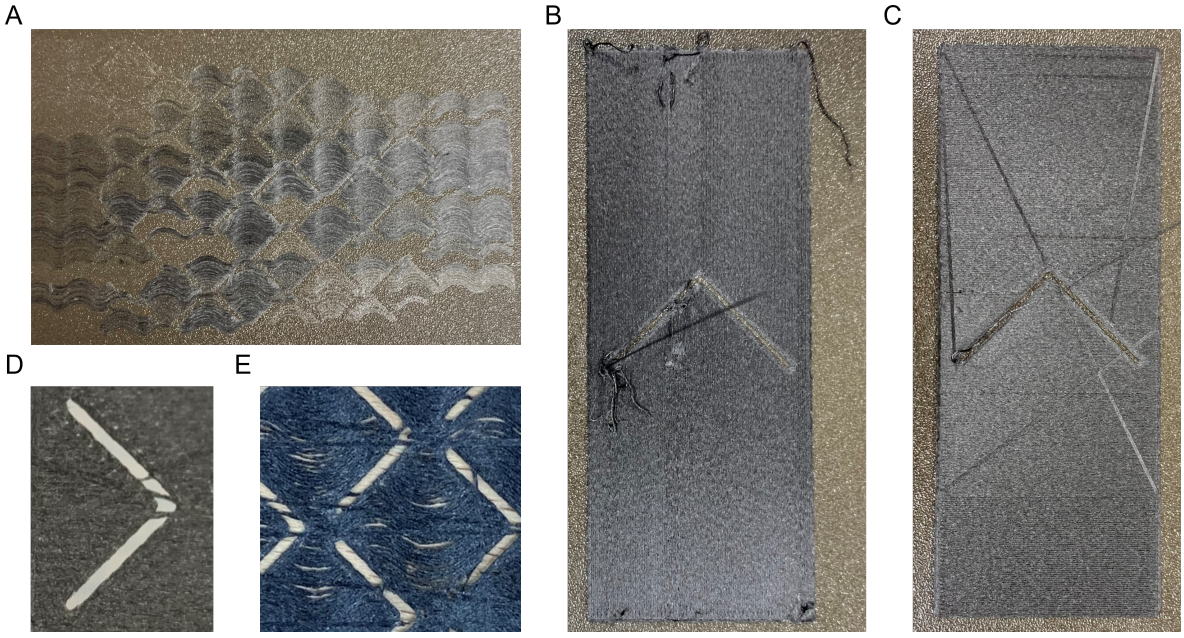

Figure 4.4: Examples of printed TPU CF specimen showing various defects. A: Print lines missing due to clogging of the nozzle. B: Unwanted material deposition due to oozing during travel motions. C: Oozing minimized by optimizing retraction- and Z-hop settings. D: Travel motions passing over the kirigami slit, resulting in partial fusion. E: Print lines not properly fused together due to under-extrusion of material.

Table 4.1: Printing parameters used to create specimen.

Parameter	Value	Unit	Parameter	Value	Unit
Print temperature	230	°C	Z-hop height	0.05	mm
Bed temperature	55	°C	Extrusion multiplyer	0.76	-
Print speed	14	mm/s	Bandwidth	0.5	mm
Travel speed	75	mm/s	Fan speed	0	%
Retraction length	5	mm	Nozzle diameter	0.4	mm

4.2. Buckled shape tests

The main aim of the buckled shape test is to find a correlation between material direction and buckled shape of the kirigami structure. With the the help of test data, the FE model will be validated.

4.2.1. Sample sizing

Five different sample groups are made for the buckled shape tests, in which either the structural parameters δ/L, γ or material orientation is varied. Thickness t, characteristic length L, slit width SW and clamp length CL are kept constant for all sample groups. All samples are printed with only one layer. Figure 4.5 shows how the material orientation is defined in the context of the kirigami structure. It can be seen that the principal direction is defined along the length of the sample.

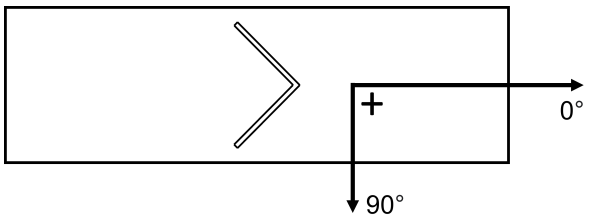

Figure 4.5: Material orientation defined in the context of the kirigami structure.

The varied parameter in the first sample group is the δ/L ratio. By increasing the value of this ratio, the hinge length will increase. The fibre direction is 0° everywhere. These samples act as a control group for the other tests that will be performed. The buckled shape should be symmetric, as the fibre pattern is unidirectional and symmetric. Therefore, the effect of other (unseen) factors will become visible, when the buckled shape deviates from a symmetric shape. These factors could originate from for example clamping conditions or printing defects. By increasing the δ/L ratio, hinge length, and thereby force required to stretch the sample, will increase. Thereby, the stress on the fixture will also increase, testing whether the fixture properly clamps samples with various geometries.

It is believed that a shape change due to varying material orientation becomes more or less apparent by changing the kirigami geometry. Therefore, the main aim of the second and third sample group is to find a correlation between the geometry and the amount of programmed behaviour. The geometric parameter δ/L is varied in the second sample group. As the UD material direction is 45°, an asymmetric buckled shape is expected that is more or less profound for samples with different δ/L ratios. The geometric parameter γ (cut angle) is varied in the third sample group. The UD material direction is 45°. Based on the same reasoning as before, an asymmetric shape is expected, that is more or less profound for samples with different cut angles γ. After the tests of the second and third sample groups are performed and analysed, a value for the δ/L ratio and cut angle γ will be chosen for which the shape change is most profound. These values are kept constant for all other tests that still have to be performed. In other words, the kirigami geometry is kept constant for the fourth and fifth sample groups.

The main aim of the last two sample groups is to find a correlation between fibre orientation and buckled shape of the kirigami structure. In the fourth sample group, the UD fibre direction is varied, the geometry of the kirigami structure is kept constant. In fifth and last sample group, all entries in the material orientation field are not equal over the entire structure (no UD fibre directions). Rather, three different symmetric field types are defined called converging-, diverging- and neutral field. All fields

have a 0° line through the centre of the kirigami structure, about which the orientation field is mirrored. The orientation fields are defined as follows from left to right:

- Converging field: +45°, 0°, -45°
- Diverging field: -45°, 0°, +45°
- Neutral field: 90°, 0°, 90°

The figures that the GCODE generation script generated, showcasing the directions of the print lines of these symmetric field samples can be seen in figure 4.6. An overview of all sample groups, the respective varied parameter, constants and manufactured samples can be seen in table 4.2. Every sample type has an identical sample count of 2.

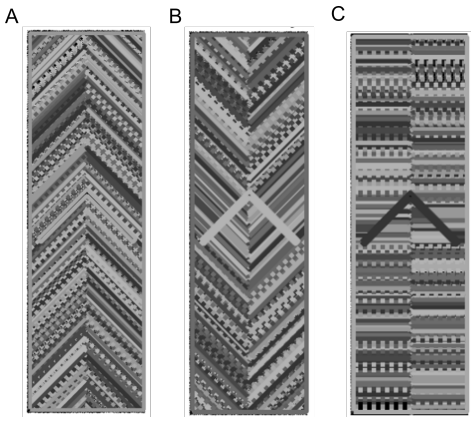

Figure 4.6: A: Print lines generated by the GCODE generation script, with the converging orientation field as input. B: Print lines generated by the GCODE generation script, with the diverging orientation field as input. C: Print lines generated by the GCODE generation script, with the neutral orientation field as input.

Table 4.2: Overview of the sample groups for the buckled shape tests, displaying the varied parameter, constants and manufactured samples.

Sample group	Varied parameter	Constants	Samples
Variable hinge length (θ_{UD} = 0°)	δ/L	t = 0.3 mm, L = 25 mm, SW = 1.15 mm, θ_{UD} = 0°, γ = 45°, CL = 30 mm	δ/L = 0.1
			δ/L = 0.2
			δ/L = 0.3
			δ/L = 0.4
			δ/L = 0.5
Variable hinge length (θ_{UD} = 45°)	δ/L	t = 0.3 mm, L = 25 mm, SW = 1.15 mm, θ_{UD} = 45°, γ = 45°, CL = 30 mm	δ/L = 0.1
			δ/L = 0.2
			δ/L = 0.3
			δ/L = 0.4
			δ/L = 0.5
Variable cut angle	γ	t = 0.3 mm, L = 25 mm, SW = 1.15 mm, θ_{UD} = 45°, CL = 30 mm , δ/L t.b.t	γ = 30°
			γ = 45°
			γ = 60°
Variable UD fibre direction	θ_{UD}	t = 0.3 mm, L = 25 mm, SW = 1.15 mm, CL = 30 mm, δ/L t.b.t., γ t.b.t.	θ_{UD} = 0°
			θ_{UD} = 30°
			θ_{UD} = 45°
			θ_{UD} = 60°
			θ_{UD} = 90°
Variable symmetric field	θ_{ij}	t = 0.3 mm, L = 25 mm, SW = 1.15 mm, CL = 30 mm, δ/L t.b.t., γ t.b.t.	Converging field
			Diverging field
			Neutral field

4.2.2. Custom fixture

The buckled shapes of the kirigami samples will be mapped with the Keyence VR-5000 microscope and analysed with corresponding software. In order to obtain reliable data, a few requirements regarding the fixture that keeps the samples in a fixed position during measurements are proposed, the reasoning behind a specific requirement can be seen between brackets:

- Distance between clamped sample and top most surface of fixture should be less than 30 mm (to prevent collision between the microscope and fixture).
- Clamp length should be 30 mm (see table 4.2).
- Fixture should be able to displace samples from 0 mm to 9.5 mm with a 0.5 mm step size (preliminary tests showed that the ultimate displacement of all samples are below 9.5 mm).
- The total length of the fixture should be able to change (to accommodate for the different sample lengths resulting from a change in cut angle γ).
- The color of the fixture should resemble the color of the samples as much as possible (preliminary tests show that the microscope is not able to properly capture dark colored surfaces (samples) when near lighter colored surfaces).
- Tolerances between moving parts should be as low as possible (the fixture should deform as little as possible when a sample is loaded).

The final design that resulted from these requirements can be seen in figure 4.7A. Clamps are mounted on a plate, by manually placing the clamps in a combination of holes, a predefined displacement of the sample is reached. The clamps are equipped with locking screws, which can be fixed in the holes in the mounting plate. A partially exploded view of the design can be seen in figure 4.7B. This figure shows that each of the clamps consists of two clamping surfaces which will squeeze the sample by manually turning two tightening screws. The top- and bottom clamp are exactly identical. The fixture design is compatible with kirigami with various overall lengths (overall length is dependent on the cut angle of the kirigami sample), through the use of a spacer with specific dimensions. By interchanging these spacers that connect both mounting plate halves, the total size of the fixture can be changed. Figure 4.7C shows both mounting plate halves along with the spacers. The hole pattern, with each hole set corresponding to a different displacement of the kirigami sample, can clearly be seen. Each set is designated with a letter such that it becomes clear which holes belong to that set. In set 'a', a displacement of 0.0 is imposed on the kirigami sample, the sample is loaded in this configuration. By displacing the clamps and stepping from set 'a' to 'b', 'c', 'd', etc, a displacement of respectively 0.5, 1.0, 1,5, etc will be reached. The pattern is made in such a way that the stepping order is from bottom to top, and consecutively from left to right.

Nearly all parts were 3D-printed using black PolyTerra PLA filament which has a matte finish. Four M6 hexagonal bolts were used as locking screws to keep the clamps in place. Furthermore, eight M6 hexagonal bolts connected the spacers to the mounting plate halves. In total, twelve holes were threaded with brass inserts, which could be inserted by locally melting the PLA with a soldering iron. This resulted in strong connections between the bolts and PLA parts. The holes in the mounting plate were not threaded. Rather, there was a very low tolerance between the locking screws and the holes, giving the clamps virtually no play once the locking screws were properly pushed in their hole set.

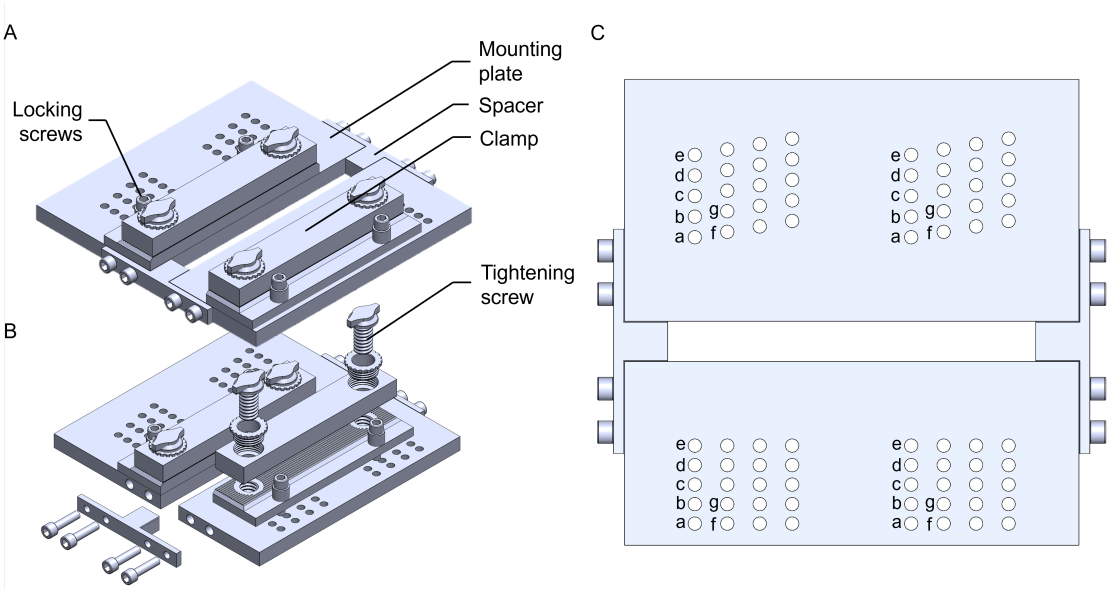

Figure 4.7: A: Design of the custom fixture for the buckled shape tests. Two clamps are mounted on a plate between which the kirigami sample is clamped, by moving the clamps to a specific hole set, a certain displacement will be imposed on the kirigami structure. By interchanging the spacers, the overall length of the custom fixture can be changed, thereby accommodating for kirigami with varying cut angle. B: Partially exploded view shows the parts in one clamp, the kirigami sample will be clamped by manually tightening the screws. The top- and bottom clamp are identical. C: Hole pattern in both mounting plate halves, each hole set (designated with a letter) corresponds to a specific displacement.

4.2.3. Height mapping

The buckled shape measurements should be taken by following this step wise approach:

1. Sample clamping: the sample is clamped in the fixture that is in its 0.0 mm displacement configuration. This is done by placing the sample between the clamping surfaces of both the top- and bottom clamp. With the help of a ruler with a 90° angle, the sample is rotated until it is perfectly aligned between the clamps. At the same time it is ensured that the top- and bottom of the sample aligns with the outer surfaces of the top- and bottom clamps. An example of a properly clamped sample can be seen in figure 4.8A.
2. Defining an area of interest: The fixture, along with the clamped sample is placed under the microscope. Reference images are taken of the sample, by using these reference images, an area of interest of the sample can be defined over which the measurement will be taken. This area of interest must be defined between the clamps. This way the measurement only consists of the sample, which makes post-processing easier. Figure 4.8B shows how the area of interest is defined. The figure indicates that a grid of 3x3 sub-measurements will be taken of this particular reference sample. The microscope will automatically focus based on the height of each subset.
3. Measurement: When the entire sample is mapped, the microscope will stitch the individual images together in order to create a smooth three-dimensional surface. When a particular measurement must be analysed, a reference surface should be defined. All out-of-plane displacements are then automatically measured from this (zeroed) surface. Figure 4.8C shows the three-dimensional surface of a sample, created by the microscope software.
4. Displacement stepping: When a measurement is taken and properly saved. A new measurement can be made. This should be done by taking the fixture from the microscope, lifting both clamps from a hole set in the mounting plates, and then pushing the locking screws into the next hole set which has a displacement which is 0.5 mm larger than the previous one.

By repeating step 2, -3 and -4, measurements are taken through an entire displacement cycle of a sample. When the sample breaks, a new sample is loaded and measured by repeating the step wise approach starting from step 1. It should be ensured that the buckling direction of the kirigami leaf is always upwards, as the buckled shapes will be compared to the buckled shapes generated by an FE model. This will be done by gently pushing the kirigami leaf in the upward direction when the buckling direction is observed to be downward.

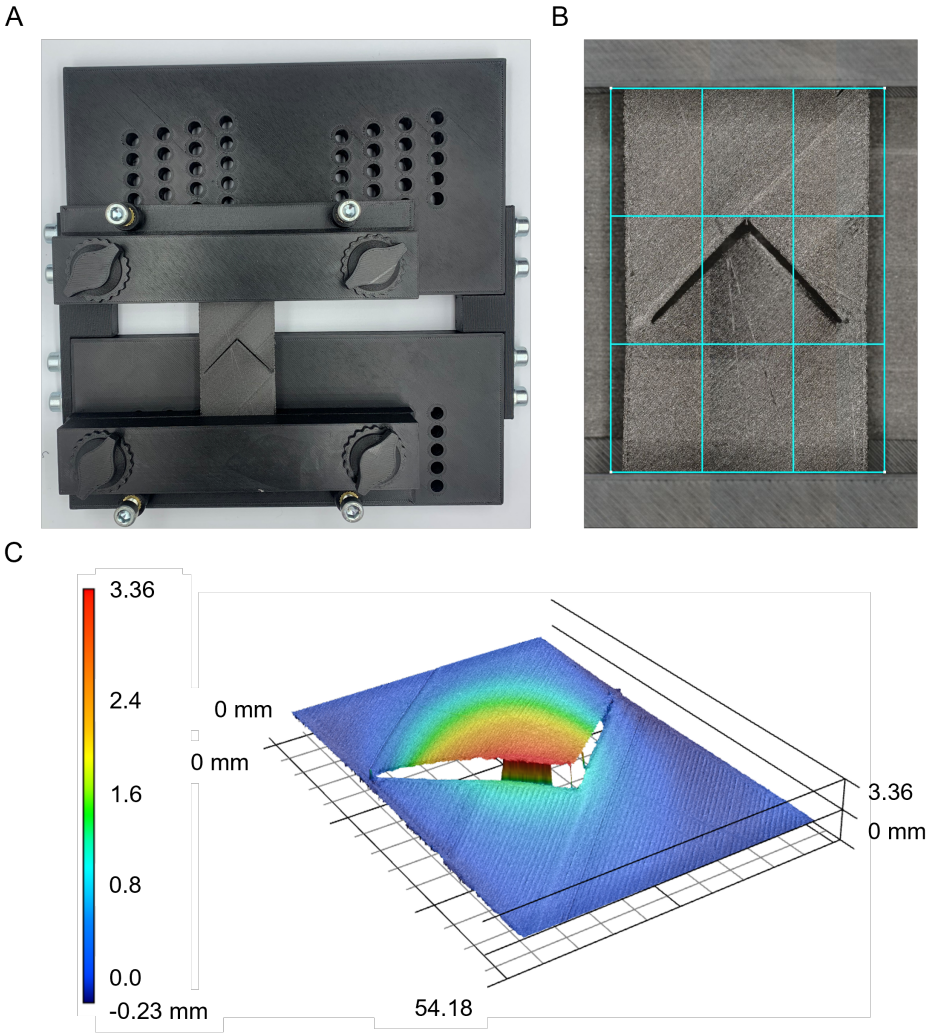

Figure 4.8: A: Example of a properly clamped sample before mapping the surface. B: Area of interest is defined between the clamps, such that the measurement only consists of the kirigami surface, in this particular example 9 sub-measurements will be taken in a grid of 3 by 3. C: After stitching the sub-measurements together, a three-dimensional surface is generated by the microscope software.

4.3. TPU CF tensile test

Tensile tests of TPU CF samples will performed to measure the mechanical properties of the material. The outcome of this test will serve as input for the FE model. The test is performed according to ISO 527-3, which describes a standardized tensile test to find the mechanical properties of anisotropic sheets with a maximum thickness of 1 mm.

4.3.1. Sample sizing and -manufacturing

Following the ISO 527-3 standard, 8 samples with 0° UD material orientation (material along the loading direction), and 8 samples with 90° UD material orientation (material perpendicular to loading direction) will be tested. The samples have a length of 175 mm, a width of 20 mm and a thickness of 0.3 mm, which will be 3D-printed with only one layer.

The samples will be manufactured by making use of the same setup and GCODE generating tool as described in subsections 4.1.1 and 4.1.3 respectively. Yet, to generate the GCODE, the mask function in the GCODE generation tool is disabled, as there are no print lines that should be omitted from the rectangular shaped samples. Only the orientation field (either 0° UD or 90° UD), defined over an 175 by 20 mm area has been used as input in the tool. Furthermore, the exact same printing settings as

listed in table 4.1 have been used to create the GCODE for the TPU CF tensile samples. By using the exact same printing parameters, it is ensured that the fibre orientations are identical (see subsection 2.3.3). Thereby, the mechanical properties of the TPU CF tensile test samples are identical to the buckled shape test samples. An example of a printed sample with 0° material orientation can be seen in figure 4.9.

Figure 4.9: A 3D-printed TPU CF sample used for measuring the mechanical properties with a tensile test. This particular sample has a UD material orientation of 0°.

4.3.2. Sample preparation and test setup

The strain in the TPU CF samples is expected to be too large for conventional strain gauges. Therefore, the three dimensional digital image correlation (3D-DIC) method is used to measure the strain in the samples. DIC essentially compares images taken during a strain cycle of a sample in order to calculate the strain. In order for the 3D-DIC system to properly track the displacement, the samples had to be covered in a speckle pattern. This speckle pattern was created by first applying a white paint, followed by a black speckle pattern which could be applied with a roller with a predefined dot size of 0.178 mm. The roller is manufactured by Correlated Solutions. An example of a TPU CF sample, after the application of the speckle pattern can be seen in figure 4.10. The choice to make use of 3D-DIC instead of 2D-DIC was essentially made because the out-of-plane thinning (ϵ_{zz}) of the samples could potentially be tracked. Unfortunately, it turned out that the setup was not accurate enough to measure this.

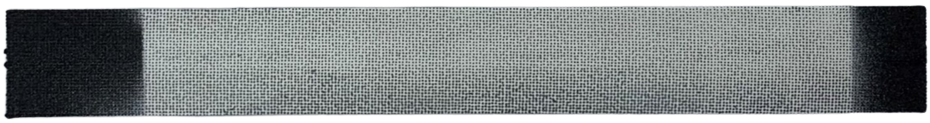

Figure 4.10: TPU CF sample after application of the speckle pattern that is required by the 3D-DIC system for proper tracking of the displacement.

A 10 kN Zwick tensile machine with a 1 kN load cell was used to test the samples. The strain rate was set to 5 mm/min. The 3D-DIC system consisted of two 9 MP cameras equipped with 50 mm focal length lenses. The cameras were placed at a 30 degree angle with respect to each other, both cameras were focused on the TPU CF samples. A floodlight was used in order to obtain adequate contrast between the white paint and black speckles. A frontal view of the entire setup can be seen in figure 4.11A.

The tensile force and bench displacement were tracked and served, along with the individual images during straining, as input for the analysis software. The VIC-3D software was used to analyse the data. The software first requires an area of interest as input over which analysis will be performed. This area was taken as large as possible, without the area going out of frame during displacement. An example of how the area of interest was defined in the context of the sample geometry can be seen in figure 4.11B. Within this area, a subset size must be defined. The subset should be large enough such that it contains enough information about the speckle pattern, but small enough such that spatial information is not lost. A subset size ranging between 30 and 40 worked for all samples. The subsets along with the speckle pattern on the sample can be seen in figure 4.11C. Lastly, a step size has to be defined. The step size controls over how many data points analysis will be performed. Lower step sizes result in longer computational times. A step size of about 25% of the subset size was used. With all inputs defined, the VIC-3D software was able to perform the analysis and calculate the strains. An example of strain in the vertical direction of a TPU CF sample just before rupture can be seen in figure 4.11D. The average strain over the area was taken and used to calculate the tensile properties of the TPU CF material.

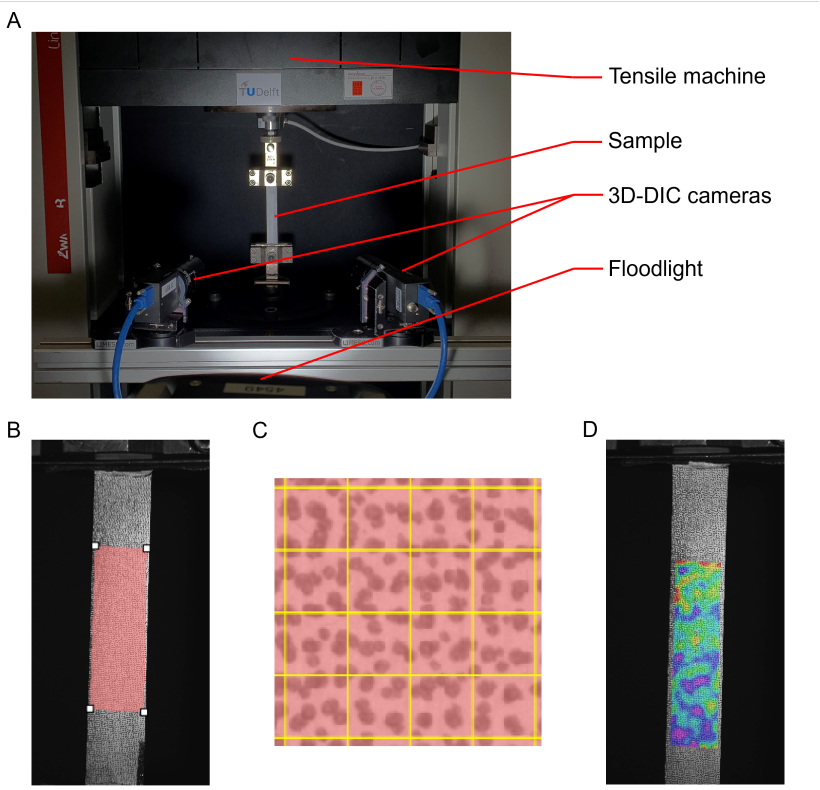

Figure 4.11: A: TPU CF tensile test with 3D-DIC setup. B: Area of interest defined on the TPU CF sample in the VIC-3D software. C: Subset size defined in the context of the speckle pattern. A subset size between 30 and 40 worked for all samples. D: Example of the strain in vertical direction just before rupture, calculated by the VIC-3D software and mapped in the area of interest.

4.4. Simulation

The programmed behaviour of the kirigami will be simulated with the help of Abaqus/CAE. After validation of the model with the help of test data, the model can be used for future research.

4.4.1. Model architecture

This section will present the structure of the Abaqus model by describing the choices and accompanying assumptions that have been made to build the model. The entire model is initiated by a Python script. This script holds all information and commands to generate a parameterized kirigami model in Abaqus.

Part

The geometry of the Abaqus part is parameterized. The geometry is created by using the exact same driving parameters and method as used in subsection 4.1.2. The section in Abaqus is defined as a homogenous shell, meaning that no numerical integration through the thickness will be performed. As the kirigami structure is essentially a thin sheet in which out-of-plane loads are low, only considering in-plane effects is a feasible assumption.

Material

As the deformation of kirigami is mainly determined by regions with low strain, the assumption is made that the material behaviour can be described by using elastic moduli approximated at the beginning of the stress-strain curve of the TPU CF material. The material model chosen in Abaqus is the 'lamina' type. By choosing this definition, the model will take the anisotropic behaviour of the material into account. Simultaneously, it will assume purely in-plane stress ($\sigma_3 = 0$). This assumption is valid, since the kirigami model was defined as a shell in which this assumption is already made. The 'lamina' material model requires the following independent properties: elastic modulus in the principal direction E_1, elastic modulus in the transverse direction E_2, Poisson ratio related to an extension in the principal

direction and displacement in the transverse direction ν_{12}, in-plane shear modulus G_{12} and transverse shear moduli G_{13} and G_{23}.

In order to define the material orientation, a discrete field is used in Abaqus. This field contains vectors which are assigned to the centroids of the mesh elements. The vectors define the orientation of the principal direction, the transverse direction is defined with a 90° angle with respect to the principal direction. The Python script is made such that it receives the coordinates of the centroids of the mesh elements. It compares this data to the user defined orientation field which is also used to generate the GCODE, as explained in 4.1.3. This orientation field is essentially a large matrix in which every entry describes the local material angle in radians. As the coordinates of the centroid of the mesh element, at which a material orientation needs to be defined, do not correspond with the coordinates of the local orientation in the orientation field, an interpolated value needs to be found. The orientation at the centroid of the mesh element can be found by using the repeated linear interpolation method, which can be described by the following equation:

$$\theta(x,y) = \frac{1}{(x_2-x_1)(y_2-y_1)} \begin{bmatrix} x_2-x & x-x_1 \end{bmatrix} \begin{bmatrix} \theta(x_1,y_1) & \theta(x_1,y_2) \\ \theta(x_2,y_1) & \theta(x_2,y_2) \end{bmatrix} \begin{bmatrix} y_2-y \\ y-y_1 \end{bmatrix} \tag{4.4}$$

The equation essentially finds a value for the orientation at the mesh element centroid $\theta(x,y)$ by comparing its coordinates (x,y) with four nearby datapoints and their respective values for the orientation ($\theta(x_1,y_1)$, $\theta(x_1,y_2)$, $\theta(x_2,y_1)$ and $\theta(x_2,y_2)$). A visual representation of the repeated linear interpolation method, along with the required values to evaluate the material orientation at the mesh element centroid can be seen in figure 4.12.

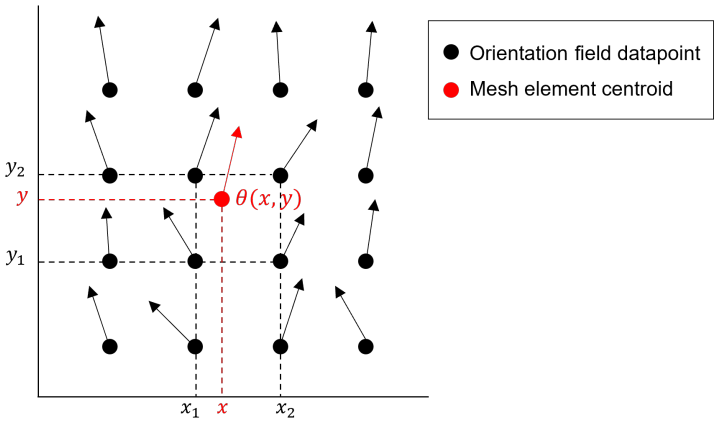

Figure 4.12: Visual representation of the repeated linear interpolation method. This method is used to find the value for the material orientation at the mesh element centroid. It does this by comparing the location of the mesh element centroid with four nearby data points and their respective values for the orientation.

Boundary conditions and steps

Two simulation steps are defined to ensure a consistent buckling direction of the kirigami structure. The kirigami leaf is the buckling surface with the largest out-of-plane deflection. However, there is another buckling surface, located just above the kirigami tip. In the first step, boundary conditions are imposed on two vertices that represent both buckling surfaces, as shown in figure 4.13A. A very small out-of-plane displacement (0.5 mm) is imposed on these boundary conditions. Furthermore, both the top- and bottom clamping surfaces are fully encastered during the first step. In the second step, boundary conditions are imposed on the top- and bottom clamp. The bottom clamp is fully encastered, the top clamp has no degrees of freedom except for the vertical direction, as indicated by 4.13B. The vertical displacement of the top clamp was typically set between 4.0 mm and 6.5 mm, as this depended on the geometry of the kirigami. The boundary conditions during both steps are chosen such that it resembles the actual buckled shape test as much as possible. By imposing both boundary conditions on and near the kirigami leaf tip, it is ensured that the buckling direction is consistent.

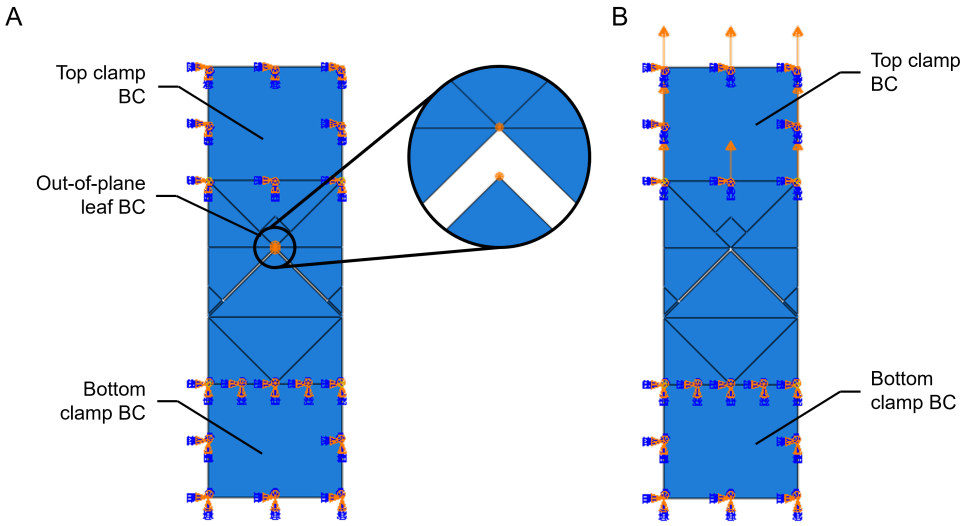

Figure 4.13: A: Boundary conditions imposed on the kirigami structure during the first analysis step. Both the top- and bottom clamping surfaces are completely encastered. To ensure a consistent buckling direction, the vertices that represent the kirigami buckling surfaces are moved out-of-plane. B: Boundary conditions imposed on the kirigami structure during the second analysis step (tensile step). Bottom clamping surface is completely encastered, top clamping surface has no degrees of freedom except for the vertical direction which is necessary to impose the displacement.

Mesh

The mesh element type is a shell element with 4 nodes and uses reduced integration to optimize computational times (S4R type). The medial axis algorithm is used to mesh the kirigami model. The kirigami model is divided over a few regions, these have specific dimensions based on the geometric input given by the user. The meshing algorithm was able to generate a smooth transition between the region boundaries, as can be seen in figure 4.14. The region boundaries are indicated with red lines.

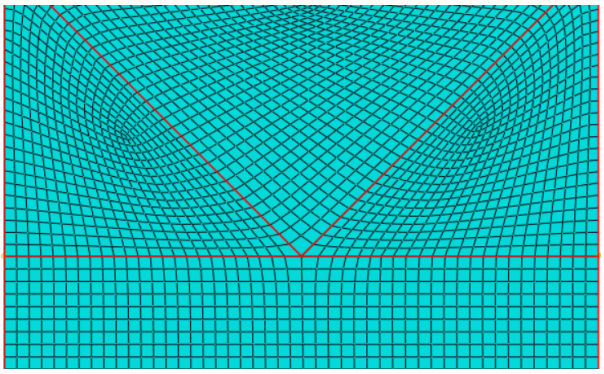

Figure 4.14: The medial axis meshing algorithm generated a smooth mesh transition between the region boundaries (indicated with the red lines). The approximate size of the mesh is set to 0.75 mm, and the mesh type is S4R.

In order to obtain accurate results while simultaneously keeping computational cost to a minimum, the mesh size has to be carefully selected. A mesh convergence study has been performed to find an optimized value for the mesh size. As the model needs to be able to capture material orientation effects, the convergence study is performed with the 45 degrees cut angle, 0.2 δ/L ratio and +45 degrees UD fibre direction sample as preliminary tests show that this sample gives a profound asymmetric out-of-plane buckling behaviour (see section 5.2.4). The convergence study starts with a mesh size of 12.5 mm and is halved for each iteration. As can be seen in figure 4.15, the finer the mesh the more profound the effect of the fibre orientation and resulting asymmetric buckled shape. This effect will plateau at around 1800 elements, which corresponds to an average mesh size of 1.57 mm. The simulated kirigami shapes that correspond to the data points in figure 4.15 are compared in appendix A

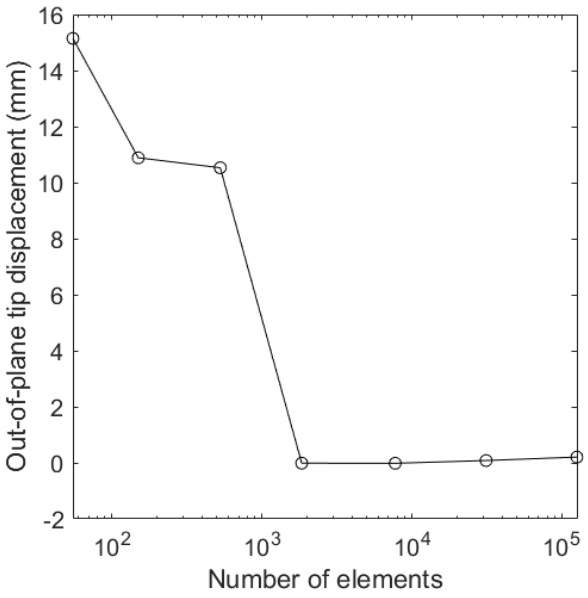

Figure 4.15: Mesh convergence study performed with 45 degrees cut angle, 0.2 δ/L ratio and +45 degrees UD material orientation kirigami sample. Comparing tip kirigami leaf tip deflection at 3.0 mm in-plane displacement. Results plateau after 1800 elements, which corresponds to an average mesh size of 1.57 mm.

4.4.2. Validation

In order to compare the FE results with actual test data, a comparison will be made by overlaying both three dimensional surfaces. The buckled shape of the kirigami FE model can be saved in an STL format and be used as input in the Keyence VR-5000 software. By opening the 'comparison' module in the software, one is able to input the STL data and overlap it with the actual sample measurement. An example of an FE result, as displayed by the Keyence software can be seen in figure 4.16A. In order to properly overlap both surfaces, some user input is required. First of all, the X- and Y- coordinates of the FE- and test results were matched by aligning the surfaces at the top vertex of the cut, as indicated by figure 4.16B. This point was chosen as its position during stretching was relatively unaffected by the fibre pattern (as opposed to the kirigami leaf tip). Secondly, the Z-coordinates (height) were matched by aligning the surfaces just inward of the top clamp. Here, the out-of-plane deflection is (nearly) equal to zero. Once the surfaces are properly overlapped, their differences become apparent. These differences can be used to make statements about the validity of the model.

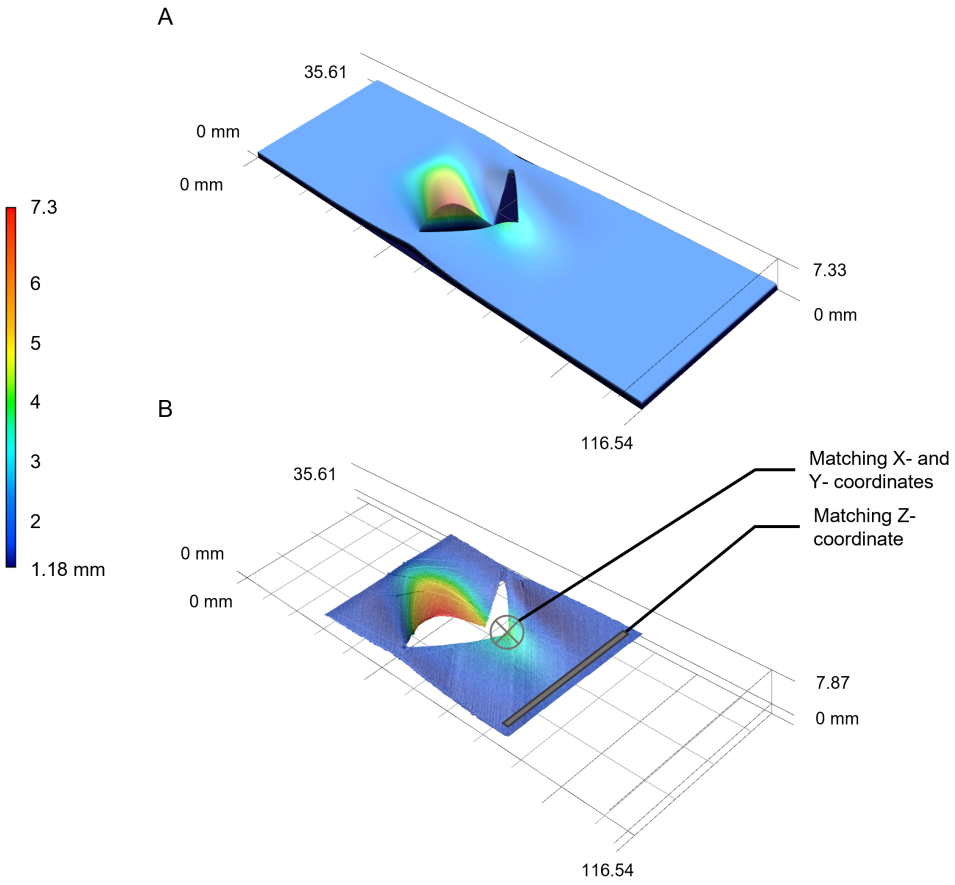

Figure 4.16: A: Example of an FE result, used to showcase the aligning approach which is used for validation of the model. B: Example of buckled shape test data. The method for aligning the FE result with the actual test data is highlighted

5

Results and Discussions

5.1. Manufacturing

In this section, the quality of the final product will be investigated. In particular, the deviation in geometric parameters of the printed samples with respect to their design will be looked into.

5.1.1. Thickness measurements

The printed samples exhibited a deviation of 0.04 mm compared to the designed thickness. In order to optimize the printing parameters for the thickness, a micrometer was used to gauge the thickness of the printed sample after each printing parameter iteration. These measurements were taken at three distinct points across the kirigami sample, as depicted in figure 5.1A. The arithmetic mean of these measurements, across all samples which were printed using the parameters as shown in tables 4.1 and 4.2 was equal to the designed thickness of 0.30 mm.

Simultaneously, measurements were made with the Keyence VR-5000 microscope to evaluate the quality of the printed sample. The thickness could be deduced by making use of the height map that resulted from these measurements. This was done by measuring the height profile of the sample across multiple straight lines perpendicular to the fibre direction/print direction (as indicated by the blue lines in 5.1B) and taking the arithmetic mean. The sample which is shown in figure 5.1B is printed with +45 degree unidirectional material orientation. An example of an average profile that resulted from such a measurement can be seen in figure 5.1C. This method was repeated for multiple samples across multiple locations over the sample. The average sample thickness that resulted from these measurements was equal to 0.26 mm. The difference in thickness between these measuring techniques mainly stem from the wavy nature of a 3D-printed layer. Micrometer measurements capture peak points of the printed lines, which will over-estimate the actual (average) thickness. This thickness discrepancy needs to be accounted for in the FE model.

The width of the peaks in the thickness profile was on average 0.31 mm in the samples with unidirectional fibre direction. This indicated that the printed lines were properly fused in most locations, as the width of the printed line was set to be 0.4 mm in the MATLAB code. There were some exceptions in which the width of the peaks was equal to the line width. Here, there was little to no fusion between the printed lines. This was caused by temporary clogging of the nozzle and happened randomly throughout the print job. Small defects were accepted as load is mainly transferred along the printed lines (stiffest path), and not between the lines. Therefore, no significant change in behaviour should be expected. If multiple, or large defects in the sample were observed, the sample was discarded.

The oozing of material out the nozzle during travel movements was reduced as much as possible by optimizing Z-hop- and retraction settings, as discussed in subsection 4.1.4. While traces of these travel motions can still be recognized in figure 5.1B, they are unlikely to alter the deformation behaviour due to their limited material deposition. Another artifact of the 3D-printing process can be recognized in figure 5.1B. The oozing caused bridges to form in the cut area, which prevented any out-of-plane

deformation when the kirigami samples were stretched. To prevent this, the lines that covered the slit were cut with a razor blade. When a print finished, the nozzle lifted from the printed structure. As there is no filament retraction present during this step, filament is left behind and causes local thickening of the sample. Which can be seen in the bottom hinge.

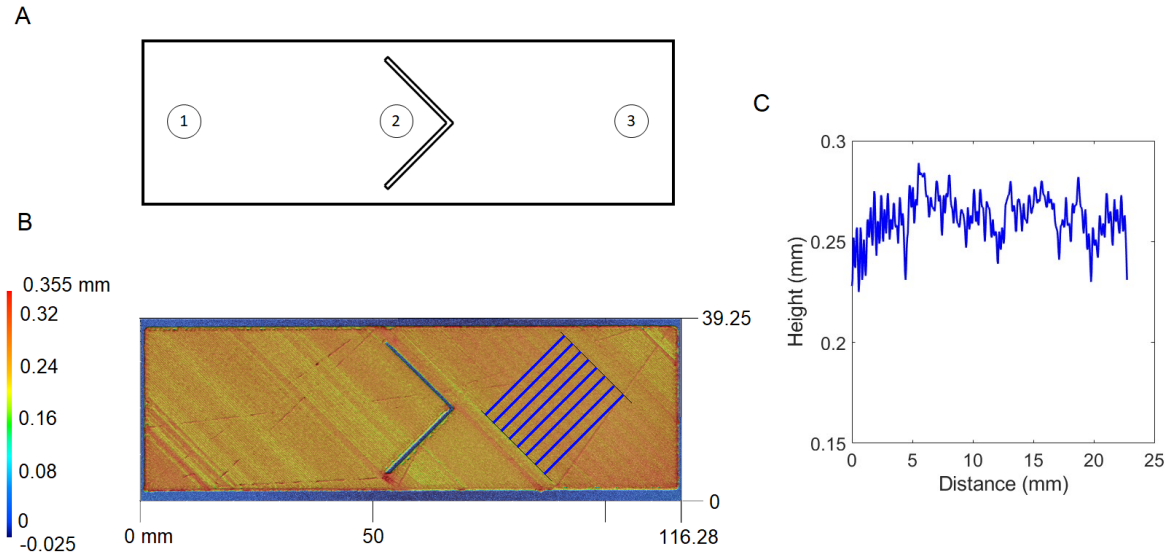

Figure 5.1: A: Three different points on the kirigami sample at which the thickness is gauged with a micrometer. The arithmetic mean of these measurements across all samples was equal to the designed thickness of 0.30 mm. B: An example of a height map measurement taken with the Keyence VR-5000 microscope of a sample with 45 degree unidirectional material orientation. The oozing of material during travel movements can be recognized across the sample. The thickness is gauged by measuring along straight lines, perpendicular to the printing direction, as indicated by the blue markings. C: An example of a thickness profile of a sample. The mean thickness derived from multiple locations across various samples is equal to 0.26 mm, which is 0.04 mm lower than the designed thickness.

5.1.2. Hinge- and slit width measurements

Also the measured hinge- and slit width deviated from their respective designed values. As shown in figure 5.2, the hinge width is found by taking the shortest distance between the edge of the sample and the slit, designated with x. The slit width is defined by SW. The Keyence VR-5000 microscope software was used to take measurements of the samples in the 0 mm displacement configuration. The arithmetic mean value for the slit width across all samples is found to be 0.53 mm, while it was designed to be 1.15 mm. The same approach was used to find the average hinge width. The value for the hinge width is not directly defined by the user. Rather, it is dependent on the δ/L ratio, which is an input to the model. The hinge width can be found by using the geometry dimension tool in Abaqus. Its value will change in the variable hinge length sample groups. The designed values, along with the measured values for the hinge width can be found in table 5.1. The hinge width of the actual samples is measured using a similar approach as for the slit width. In order to account for the deviations in geometry of the printed samples in the FE model, a corrected δ/L value is found, as can be seen in table 5.1.

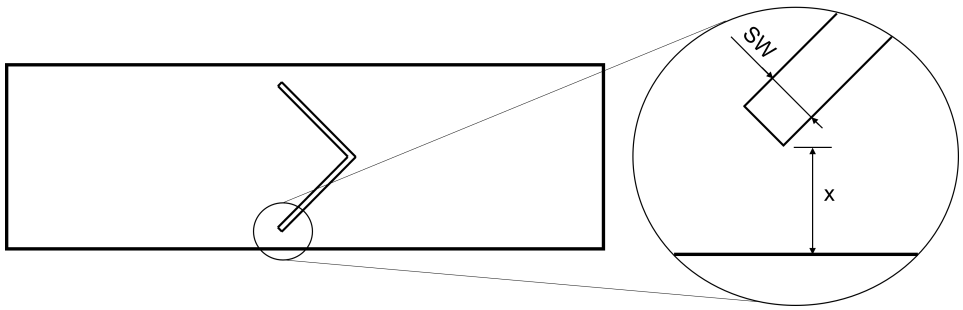

Figure 5.2: Definition of the slit width SW and hinge width x in the context of the kirigami structure.

Table 5.1: The designed- and measured values for the hinge width x, the values hold for different values of the δ/L ratio. To account for the deviation a corrected δ/L ratio is found.

	δ/L 0.1	δ/L 0.2	δ/L 0.3	δ/L 0.4	δ/L 0.5
x, designed (mm)	1.387	3.154	4.922	6.690	8.458
x, measured (mm)	2.059	3.702	5.608	7.513	9.066
Corrected δ/L value	0.138	0.231	0.339	0.447	0.535

5.2. Buckled shape tests

5.2.1. Effect of the hinge length

Samples were tested with five δ/L ratios ranging from 0.138 to 0.535. In order to compare the shapes of kirigami samples, analysis was done on measurements at a displacement of 2.0 mm. This ensured a relatively low effect of pre-stress that could be introduced when clamping the sample, while simultaneously ensuring that there is no plastic deformation present in the sample (the ultimate displacement was 4.0 mm or higher for all samples). Next, an area of interest was defined around the leaf of the kirigami, as indicated by the dashed line in figure 5.3A. The front view of this section was taken for all measurements and the resulting shapes are overlaid. The first sample group had 0 degrees UD material orientation (figure 5.3B), while the second sample group had an off-axis UD material orientation of +45 degrees (figure 5.3C). The 0 degree UD sample group was used as a control group, to show the testing setup would not bias the samples into a certain (asymmetric) shape. As expected, the 0 degree UD samples all showed symmetric out-of-plane deformation. This means that the out-of-plane deformation is largest at- and symmetric around- the tip of the kirigami leaf. Therefore, it can be concluded that the testing setup, or any other unforeseen factors, will not affect the buckled shape of the kirigami structure. The +45 degrees samples do show asymmetric out-of-plane behaviour. The point at which out-of-plane deformation was largest (peak), shifted towards the right, following the material orientation. This behaviour was observed for all samples in the +45 degree orientation group except for the sample with a δ/L ratio of 0.138. In this sample, some asymmetric behaviour was observed. However, the peak aligned with the tip of the leaf. The samples with δ/L ratio larger than 0.138 all showed similar asymmetric out-of-plane behaviour. Yet, the total out-of-plane deformation decreased with increasing δ/L ratio. For this reason a δ/L ratio of 0.231 was chosen for all samples that still had to be tested.

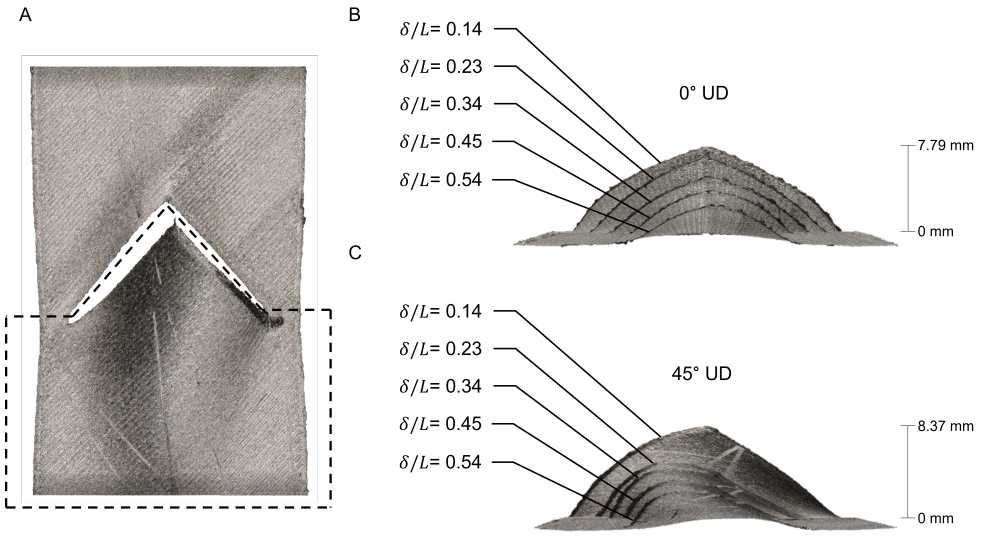

Figure 5.3: A: The dashed line shows the area of interest defined in the context of the geometry of the δ/L 0.23 sample at 2.0 mm displacement. B: Front view of the area of interest. Shapes with varying δ/L ratio are overlaid to showcase their differences. The shapes are observed to be symmetric for the 0 degree UD sample group. C: Similar to B, however, the material direction is +45 degrees. The shapes are observed to asymmetric.

5.2.2. Effect of cut angle

Samples were tested with a cut angle of 30, 45 and 60 degrees and material orientation of +45 degrees. As discussed in subsection 5.2.1, all samples had a δ/L ratio of 0.231. Again, to ensure valid results, analysis is done on measurements related to the 2.0 mm displacement configuration. A height map of the buckled kirigami was taken such that their shapes could be compared. The results of the samples with 30-, 45-, and 60- degree cut angle can be seen in figure 5.4A, 5.4B and 5.4C respectively. All samples show asymmetric out-of-plane behaviour. Yet, this behaviour is most significant in the 30- and 45- degree cut angle samples. Because the 45 degree cut angle sample shows a more significant out-of-plane deformation compared to the 30 degrees sample, a 45 degree cut angle is chosen for all samples that still had to be tested.

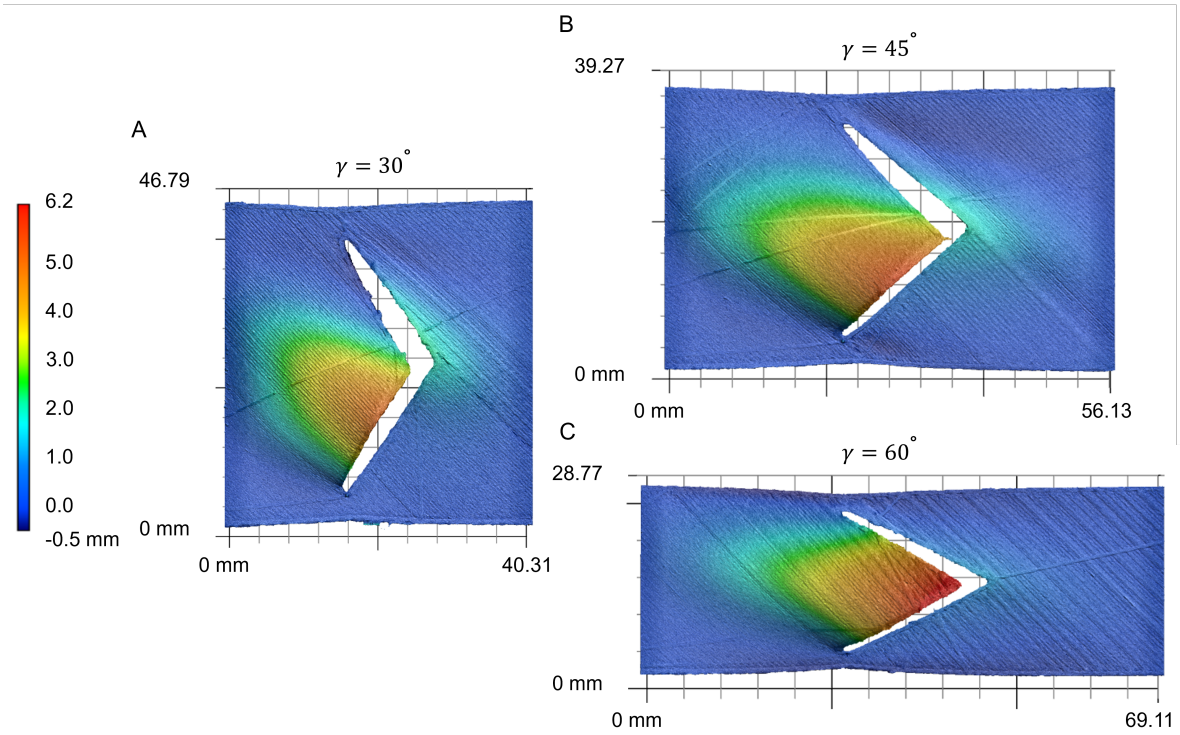

Figure 5.4: A: Height map of a sample with +45 degrees material orientation and 30 degrees cut angle in the 2.0 mm displacement configuration. The out-of-plane deformation is asymmetric. B: Height map of a sample with +45 degrees material orientation and 45 degrees cut angle in the 2.0 mm displacement configuration. The out-of-plane deformation is asymmetric. C: Height map of a sample with +45 degrees material orientation and 60 degrees cut angle in the 2.0 mm displacement configuration. The asymmetric out-of-plane deformation is not as significant as the other samples.

5.2.3. Predicting buckled shapes

Kirigami structures will invert a global uniaxial stretch in a local compression of the kirigami leaf, this compression will cause local buckling of the kirigami leaf. As a kirigami structure is in essence a thin sheet, classical plate buckling theory can be used. By following this theory, predictions about the shape of a buckled kirigami structure with specific material orientation can be made. Two rules are posed by following this theory:

1. A thin plate with clamped sides under compression will buckle in the shape of a smooth parabola with the peak in the centre. The path, over which this parabola shape with most significant out-of-plane deformation is projected is highlighted in red in figure 5.5A.
2. The steepness of the buckled parabola is directly proportional to the local directional stiffness of the material. Naturally, the path with most significant out-of-plane deformation is the path of least resistance (i.e. lowest bending stiffness). As the bending stiffness is proportional to material stiffness, and the programmed kirigami exhibits variable stiffness, this projected path will change based on material orientation. The projected path will follow the direction perpendicular to the printing direction, as this direction has the lowest stiffness. The buckled shape that will result by

compressing a thin plate in the middle, with the edges simply supported, can be seen in figure 5.5B. The sample shown in this figure has an off-axis material orientation, resulting in a buckled shape that no longer aligns with the compression force.

Two different shapes will result from rule 1 (based on kirigami geometry and boundary conditions) and rule 2 (based on material orientation). As the boundary conditions of the kirigami leaf in the context of the entire kirigami structure is not simply supported and not fully clamped, but rather a condition in between, the shape that the kirigami structure will eventually exhibit is a superposition of both shapes. The results that follow from the buckled shape tests will be analysed by following both rules as stated above.

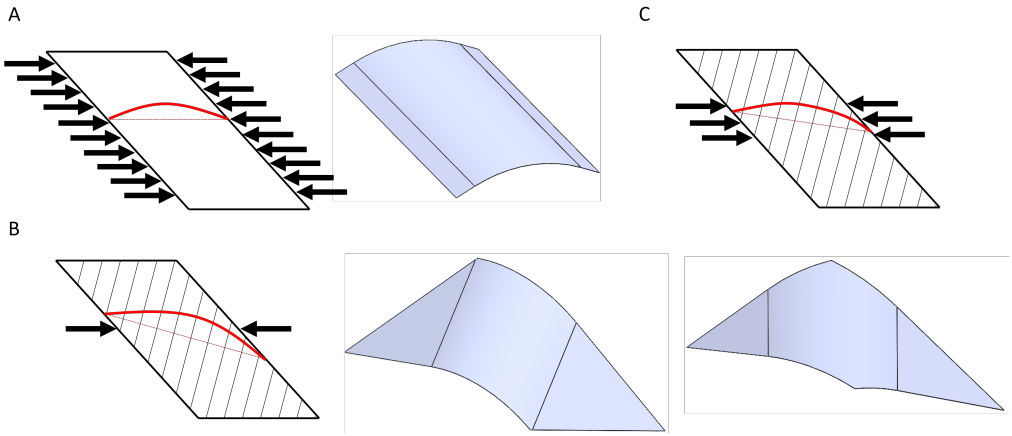

Figure 5.5: A: Plate under compression will buckle. The resulting buckled shape will be symmetric. B: Simply supported plate under compression with an off-axis material orientation will buckle in a shape that does not align with the compression force. C: As the boundary conditions of the kirigami leaf in the context of the entire kirigami structure is not simply supported and not fully clamped, but rather a condition in between, the shape that the kirigami structure will eventually exhibit is a superposition of both shapes.

5.2.4. Effect of UD fibre direction

Samples with 0, +30, +45, +60 and 90 degree unidirectional fibre direction were tested. The samples had a δ/L ratio of 0.231, and a cut angle of 45 degrees. Samples with these values seemed to be most affected by a change in material orientation according to subsection 5.2.1 and subsection 5.2.2. To ensure valid results, analysis was done on the measurements of the samples in 2.0 mm displacement configuration. A height map of the buckled kirigami was taken such that their shapes could be compared. The height map of the samples with 0, +30, +45, +60 and +90 UD fibre direction can be seen in figure 5.6A, 5.6B, 5.6C, 5.6D and 5.6E respectively. As can be seen in the figure, all samples with an off-axis material orientation (+30, +45 and +60 degrees) material orientation show asymmetric out-of-plane behaviour. This effect is most significant for the +45 degree sample. Here, a retracting motion of the leaf tip can be observed. This is not, or to a very limited extent, the case for the other samples. It is interesting to note that the 0- and 90 degree samples show a different symmetric buckled shape. Where the out-of-plane deformation in the 0 degrees sample covers a large part of kirigami structure, the deformation in the 90 degrees sample seems to mainly occur locally in the leaf. This is a direct result of the stiffness variation in the direction of compression, as stated by rule 2 in 5.2.3. The stiffness in the direction of compression in the 90 UD sample is higher compared to the 0 UD sample. Naturally, the 0 UD sample shows deformation that not as localized around the kirigami leaf. Interestingly, the buckled shape of the +60 UD sample is less asymmetric compared to the +45 UD sample. By taking rule 2 into account, one would expect the +60 UD sample to have a buckled shape that is more skewed. It seems that the material, that is providing the compression and is located around the buckled leaf, is too stiff, and is thereby not allowing the buckled shape (displayed by the material orientation) to properly form. Lastly, it can be observed that the out-of-plane deformation is smallest in the +45 sample, the sample for which the asymmetric out-of-plane behaviour is most significant. A possible explanation might be that a fairly large portion of the total strain is in-plane (retraction of the leaf tip) rather than mostly out-of-plane, as is the case for for example the 30- and 60 degree samples.

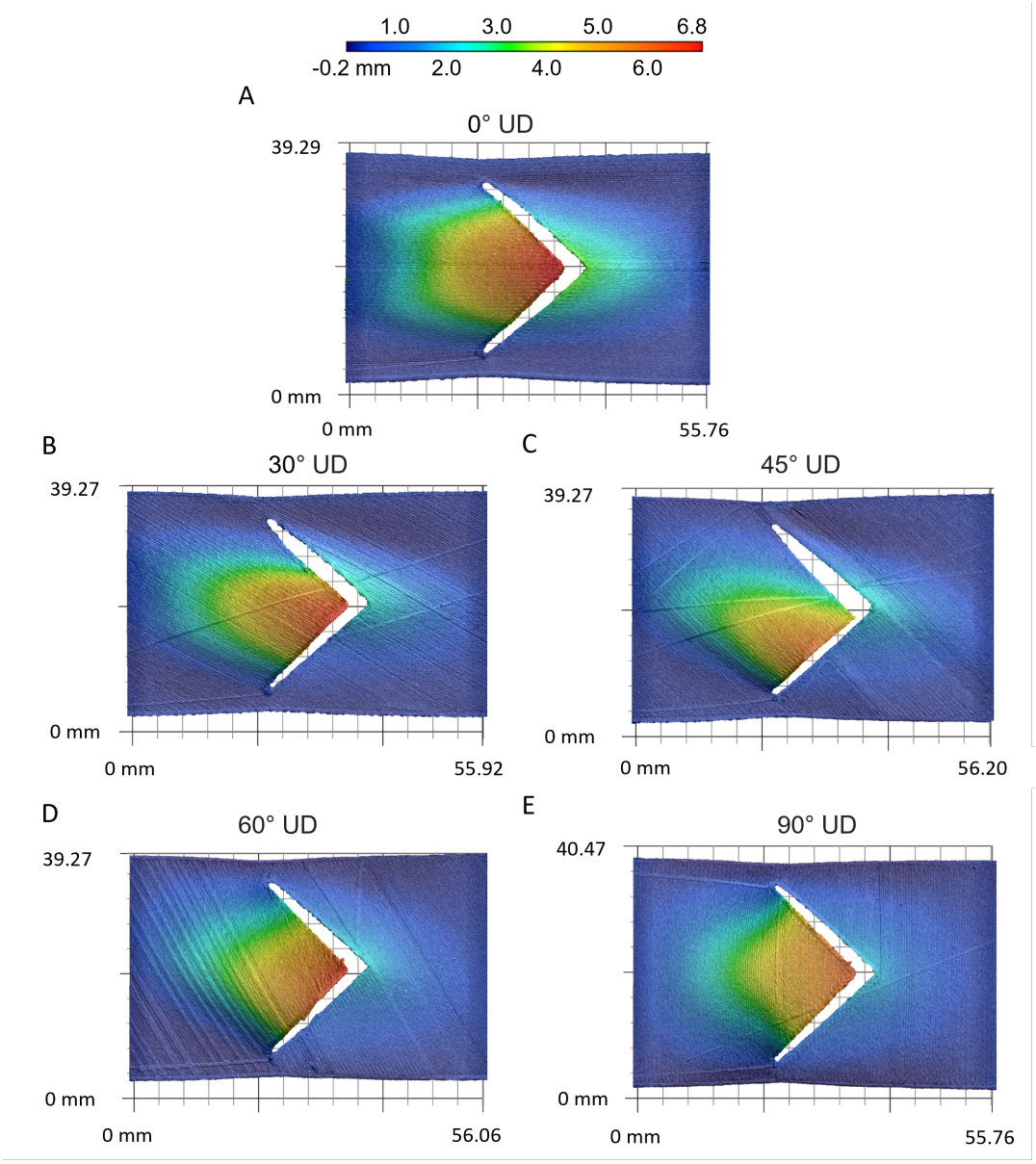

Figure 5.6: A: Height map of a sample with 0 degrees material orientation in the 2.0 mm displacement configuration. The out-of-plane deformation is symmetric. B: Height map of a sample with +30 degrees material orientation in the 2.0 mm displacement configuration. The out-of-plane deformation is slightly asymmetric. C: Height map of a sample with +45 degrees material orientation in the 2.0 mm displacement configuration. The sample shows significant asymmetric out-of-plane behaviour. D: Height map of a sample with +60 degrees material orientation in the 2.0 mm displacement configuration. The out-of-plane deformation is slightly asymmetric. E: Height map of a sample with 90 degrees material orientation in the 2.0 mm displacement configuration. The out-of-plane deformation is symmetric and more locally present near the kirigami leaf compared to the 0 degrees sample.

5.2.5. Effect of symmetric orientation fields

The last sample group that was tested had a converging-, diverging- and a neutral orientation field. These fields changed orientation about the centre of the kirigami sheet with a 0 degree line. The converging field had +45 and -45 degree material orientation on respectively the left- and right side of the kirigami sheet, as shown in figure 5.7A. This material orientation was reversed in the diverging field sample such that it had -45 and +45 degree material orientation on respectively the left- and right side. The material orientation in the neutral field sample was 0 degrees on both kirigami halves. Again, to ensure valid results, analysis is done on measurements related to the 2.0 mm displacement configuration. A height map of the samples with converging- diverging- and neutral material orientation field are shown in figure 5.7A, 5.7B and 5.7C respectively. The neutral orientation field shows the

least out-of-plane deformation. As the material is relatively stiff in the direction of compression, this could be expected. All buckled shapes are very similar, however upon close inspection it can be seen that the converging field sample shows a more gradual increase in out-of-plane deformation when moving in the compression direction towards the middle of the sample. This is also to some degree the case for the diverging field sample. Yet, the neutral field sample shows a more localized out-of-plane deformation in the kirigami leaf compared to the other samples. These samples do not show very significant differences, although their respective orientation fields are different. As there are multiple material orientations present in each sample, there are multiple preferred buckled shapes across the sample. Possibly, these shapes cancel out, and the preferred buckled shape resulting from the kirigami geometry will predominate. With this reasoning, small deviations in this buckled shape are possible (as can be seen in the results). However, these small deviations are very hard to predict beforehand, as they follow from the intricate merging of various shapes in the samples. A finite element model might be able to simulate this behaviour.

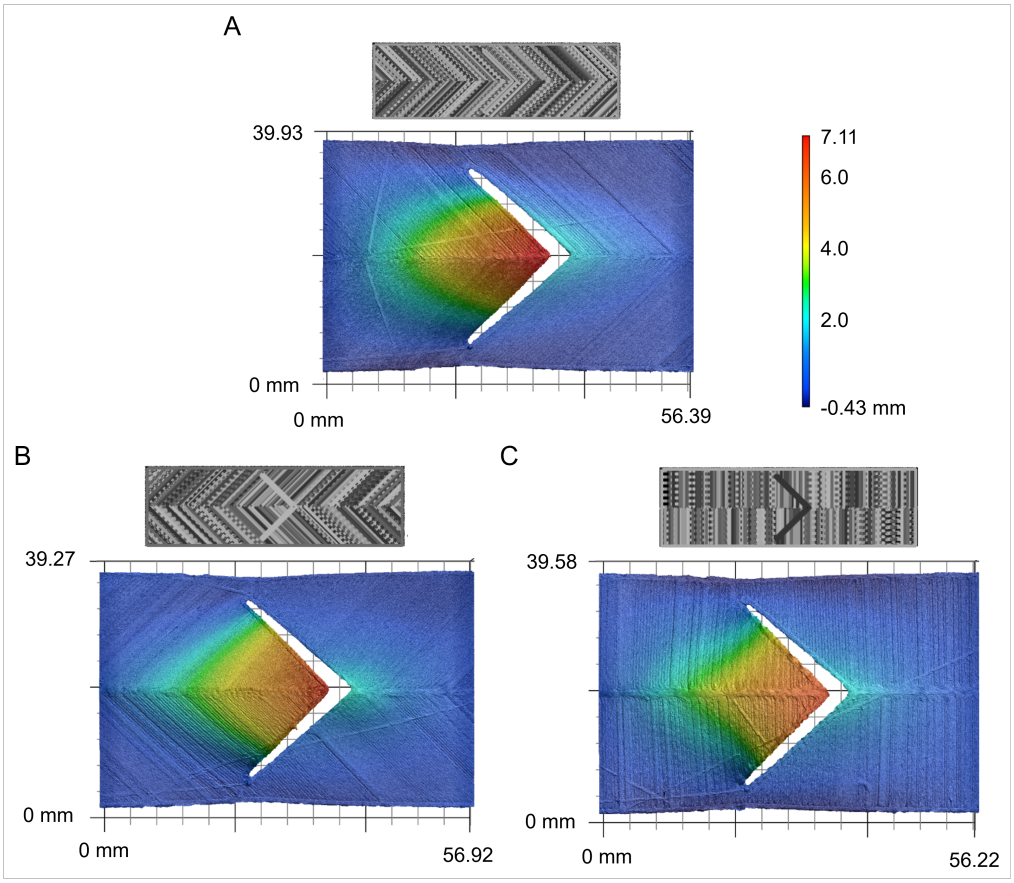

Figure 5.7: A: Height map of the converging field sample at 2.0 mm displacement. B: Height map of the diverging field sample at 2.0 mm displacement. C: Height map of the neutral field sample at 2.0 mm displacement.

5.3. TPU CF tensile test

5.3.1. Main characteristics

Mechanical tests were performed to find the tensile properties of the TPU CF material, these findings will serve as input for the FE model. Figure 5.8 shows the stress - strain curves of samples loaded in the 0 degrees material orientation, and samples loaded in the 90 degrees material orientation. As expected, the stiffness in the longitudinal direction is significantly higher compared to the lateral direction. Furthermore, it can be seen that the TPU CF material behaves like a hyperelastic material in both directions. Also this could be expected, since TPU is an alternative to rubber that is compatible with the fused filament fabrication process. The addition of carbon fibres do not seem to change this behaviour. As discussed in subsection 2.1.1, the strain in ribbon type kirigami structures is very dis-

tributed over its area. Its deformation behaviour is thus mainly determined by regions in which the strain is low. Therefore, linear approximations of the mechanical properties of the material can be made. These approximations are the elastic moduli in the longitudinal- and lateral direction, and are equal to respectively 815 MPa and 62.5 MPa. By taking another close look at figure 5.8, it can be seen that the curves do not start in the origin. It could be the case that the 3D-DIC software was not able to capture small strains. However, this inaccuracy will not influence the approximations for the elastic moduli significantly.

As 3D-DIC was used, the strain in the x-direction could also be measured (lateral thinning). Therefore, the Poisson ratios ν_{12} and ν_{21} could be calculated by evaluating the strain in both directions for in the 0- and 90 degree samples. The Poisson ratio - strain curve that resulted from these calculations can be seen in figure 5.9. Interestingly, the Poisson ratio of most 0 degree samples (ν_{12}) is larger than 0.5 for the initial 50% of the stretch cycle. This is in contrast to the behaviour observed in the 90 degree direction. Here, the Poisson ratio is constant and close to zero. Most materials experience an increase in volume when stretched, these materials have a Poisson ratio ranging between 0 and 0.5. However, as can be concluded from figure 5.9 this behaviour will change through the addition of fibres in the material. As the only physical property that changed between the 90- and 0 degree samples is fibre direction. An approximation is made for the ν_{12}, as the FE material model requires this as an input. The approximation is made at the beginning of the Poisson ratio - strain curve, as the kirigami deformation behaviour is mainly determined by regions with low strain, and is equal to $\nu_{12} = 0.7$.

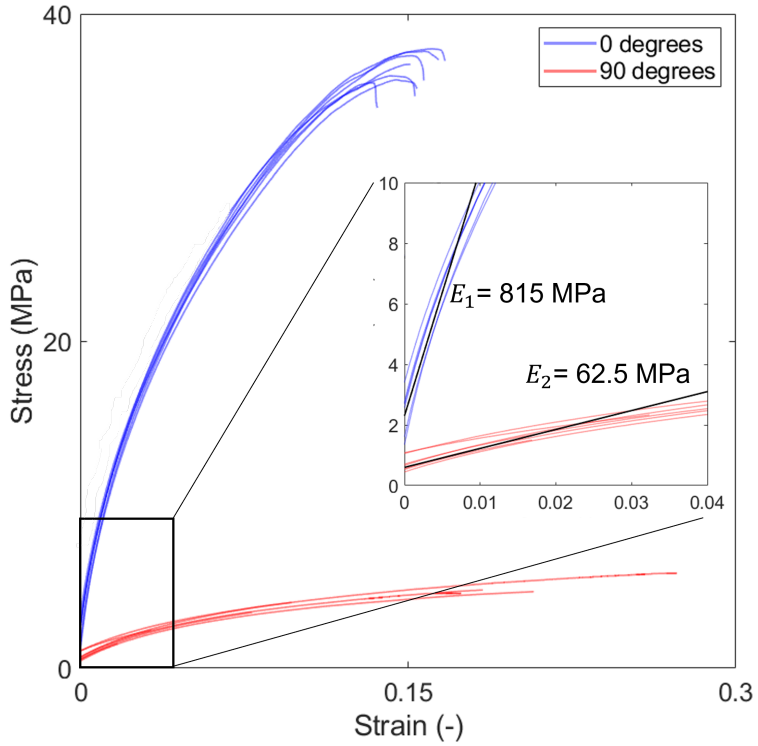

Figure 5.8: Stress - strain curve of TPU CF samples loaded in the 0- and 90 degree material orientation. Material behaviour is hyperelastic in both directions. As expected, the stiffness in the longitudinal direction is significantly larger than in the lateral direction. A linear approximation for the stiffness is made at the beginning of the stress - strain curve in both directions, these values serve as input for the FE model.

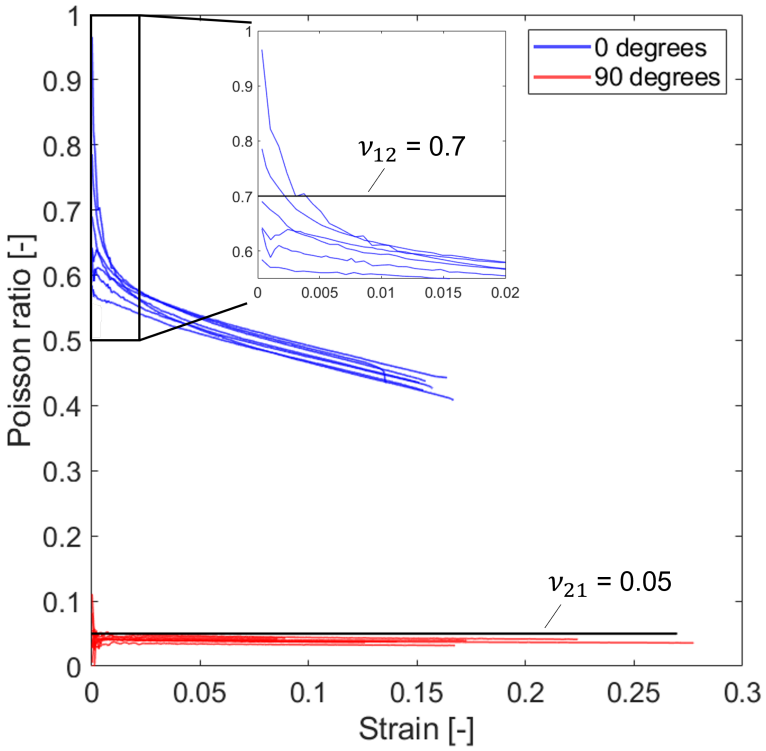

Figure 5.9: Poisson ratio - strain curve of TPU CF samples loaded in the 0- and 90 degree material orientation (ν_{12} and ν_{21} respectively). ν_{12} is larger than 0.5 for small strains and drops below 0.5 after about 50% of its stretch cyle. An approximation for ν_{12} is made at the start of the Poisson ratio - strain curve and is equal to 0.7. This value will serve as input for the FE model. ν_{21} is constant and equal to 0.05 on average.

5.3.2. Effect of paint

As the DIC software required a white sample with a black speckle pattern, the samples were covered with paint. The paint could potentially (chemically) softened the samples, and thereby influence the stiffness. In order to check whether this is the case, an unpainted sample with 0 degrees material orientation was tested, and compared to the DIC data of the 0 degrees painted samples. As the DIC system could not be used to check the strain for the unpainted sample, bench data was used. The result can be seen in figure 5.10. The curve of the unpainted sample starts in the origin. Yet, it can be seen that the stiffness of the unpainted samples is comparable to the stiffness of the painted samples. Therefore the linear approximation which is made for the elastic modulus at low strain is valid.

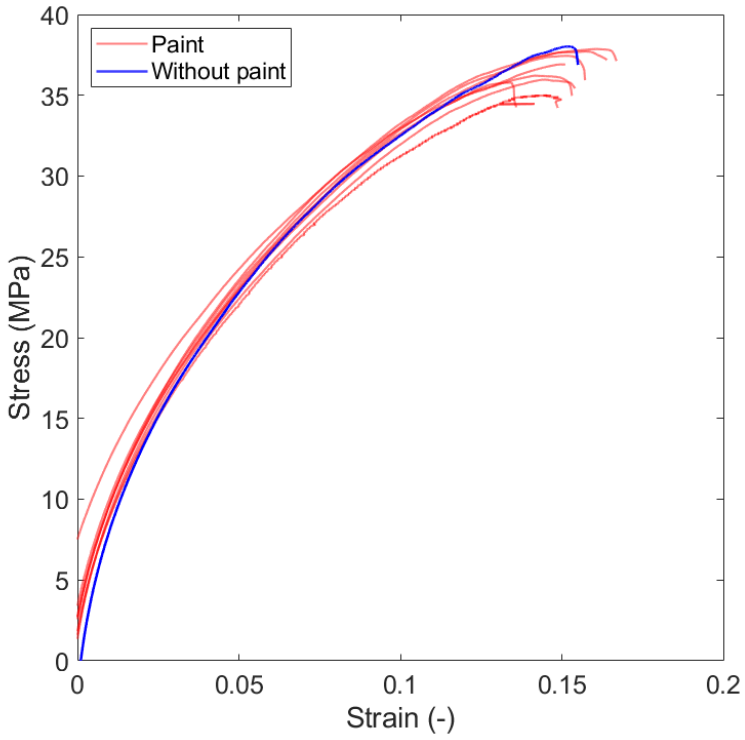

Figure 5.10: Stress - strain curve of painted- and unpainted 0 degree TPU CF sample(s). The stiffness of the unpainted sample is comparable to stiffness of the painted samples.

5.4. Simulation

5.4.1. Material model

Tensile tests have been performed to find the mechanical properties of the TPU CF material, with this data, the material model which serves as input for the FE model, can be made. As the shear moduli can not be deduced from the TPU CF tensile test data, an approximation is made. First of all, the assumption is made that the value for in-plane shear modulus G_{12} is equal to G_{13}. The 2- and 3 direction are both the lateral direction to the fibre direction. That the fibre direction with respect to these lateral directions is very comparable is a feasible assumption. In order to approximate the shear moduli, the values of other fibre reinforced composites are used for reference [50–52]. The values that are thereby found are: $G_{12} = 40\ MPa$, $G_{13} = 40\ MPa$ and $G_{23} = 5\ MPa$. The material properties input for the FE model are summarized in table 5.2.

Table 5.2: FE material model properties input

	E_1 (MPa)	E_2 (MPa)	ν_{12} (-)	G_{12} (MPa)	G_{13} (MPa)	G_{23} (MPa)
Value	815	62.5	0.7	40	40	5

5.4.2. Validation

In order to validate the FE model, its results are compared to actual test data. First of all, the out-of-plane displacement of the kirigami leaf tip is compared

Out-of-plane tip displacement comparison

Since the variable UD fibre directions samples with an off-axis material orientation show significant asymmetric out-of-plane deformation. The kirigami leaf tip deflection of this sample group will be extracted from the test data and compared to the FE results. This way it can be determined if the FE model is able to properly simulate the asymmetric out-of-plane deformation. The tip deflection comparison between the actual sample data points and the FE result can be seen in figure 5.11. It can be seen

that the FE model is able to provide a good fit for the sample data points, it is thereby able to capture the decaying rate of out-of-plane deformation for larger in-plane displacements. Furthermore, figure 5.11C shows that the FE model does capture the retracting tip motion of the +45 degree UD sample. However, the FE model is overestimating the effect. The entire out-of-plane behaviour of fibre steered kirigami cannot be captured by tracking a single point (kirigami leaf tip). Therefore, the entire buckled shape of the kirigami structure will be compared with actual test data.

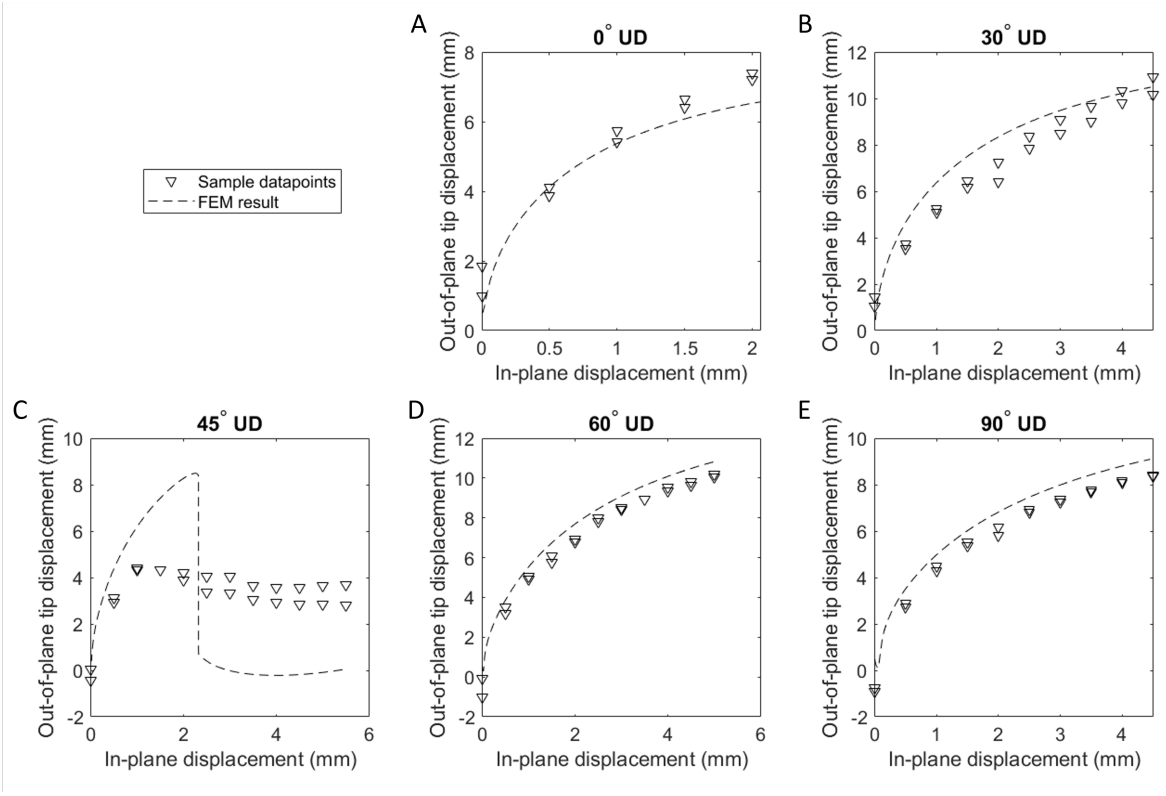

Figure 5.11: Kirigami leaf tip deflection for the UD fibre direction sample group. Comparison between FEM result and actual sample tests. The FE model provides a good fit for the actual sample data points. It can be seen that the model captures the retracting motion of the leaf tip, however it overestimates this effect.

Shape comparison

The second part of the validation of the FE model will be performed by comparing the simulated three dimensional shape with the actual test data of a sample with identical geometrical features and material orientation. With the help of the 'compare' function in the Keyence VR-5000 software, both surfaces can be overlaid and thereby be compared. Again, the validation is done for measurements taken at the middle of a displacement cycle. This way the relative effect of pre-stress is as low as possible, while simultaneously ensuring that there is no plastic deformation present in the sample. Furthermore, the validation is done for the variable UD fibre direction-, and varying orientation field sample groups. As the effect of fibre direction is captured by these two sample groups. In order to quantify how well the FE data compares to the actual test data, the error, defined by the relative deviation in out-of-plane displacement between both results, will be used. The results can be seen in table 5.3.

The results obtained after overlaying the surfaces of the 6 samples with largest deviation in out-of-plane deformation (error) can be seen in figure 5.12. Each sub-plot shows the measured three dimensional shape, FE result and the overlaid result. This surface represents the actual test data on which the deviation with respect to the FE data is projected, the scale represents the value of the deviation. When comparing the displayed three dimensional shapes of the actual test and FE result in figure 5.12, it can be seen that the FE result approaches the test data surface. As discussed in subsections 5.2.3, 5.2.4 and 5.2.5, the buckled shapes are dependent on the local stiffness of the material in compression direction. Hereby, the 0 degree UD sample had a more dispersed out-of-plane

deformation compared to the 90 degree UD sample. This effect is captured by the FE model. As discussed, the tip deflection deviation between actual data and the FE model for the 45 degree UD sample was significant. This can also be seen in figure 5.12B where the kirigami leaf tip is surrounded by a dark red colour. Yet, the asymmetric shape that the actual data shows, is approached by the FE result.

Table 5.3: Validation results by comparing maximum out-of-plane displacement of actual test data with FE data

Sample	Displacement (mm)	Out-of-plane displacement test data (mm)	Out-of-plane displacement FE data (mm)	Largest local difference (mm)	Error (%)	Figure
0 degrees UD	1.5	6.70	5.95	1.12	10.97	5.12A
+30 degrees UD	2.0	8.16	8.53	2.27	4.34	-
+45 degrees UD	2.5	7.68	7.29	2.18	5.08	5.12B
+60 degrees UD	2.5	8.56	9.27	-0.90	7.66	5.12C
90 degrees UD	2.5	7.59	8.19	-0.77	7.33	5.12D
Converging field	2.0	8.49	9.84	-1.42	13.72	5.12E
Diverging field	2.0	6.68	6.97	0.70	4.16	-
Neutral field	3.0	8.78	9.95	-1.24	11.76	5.12F

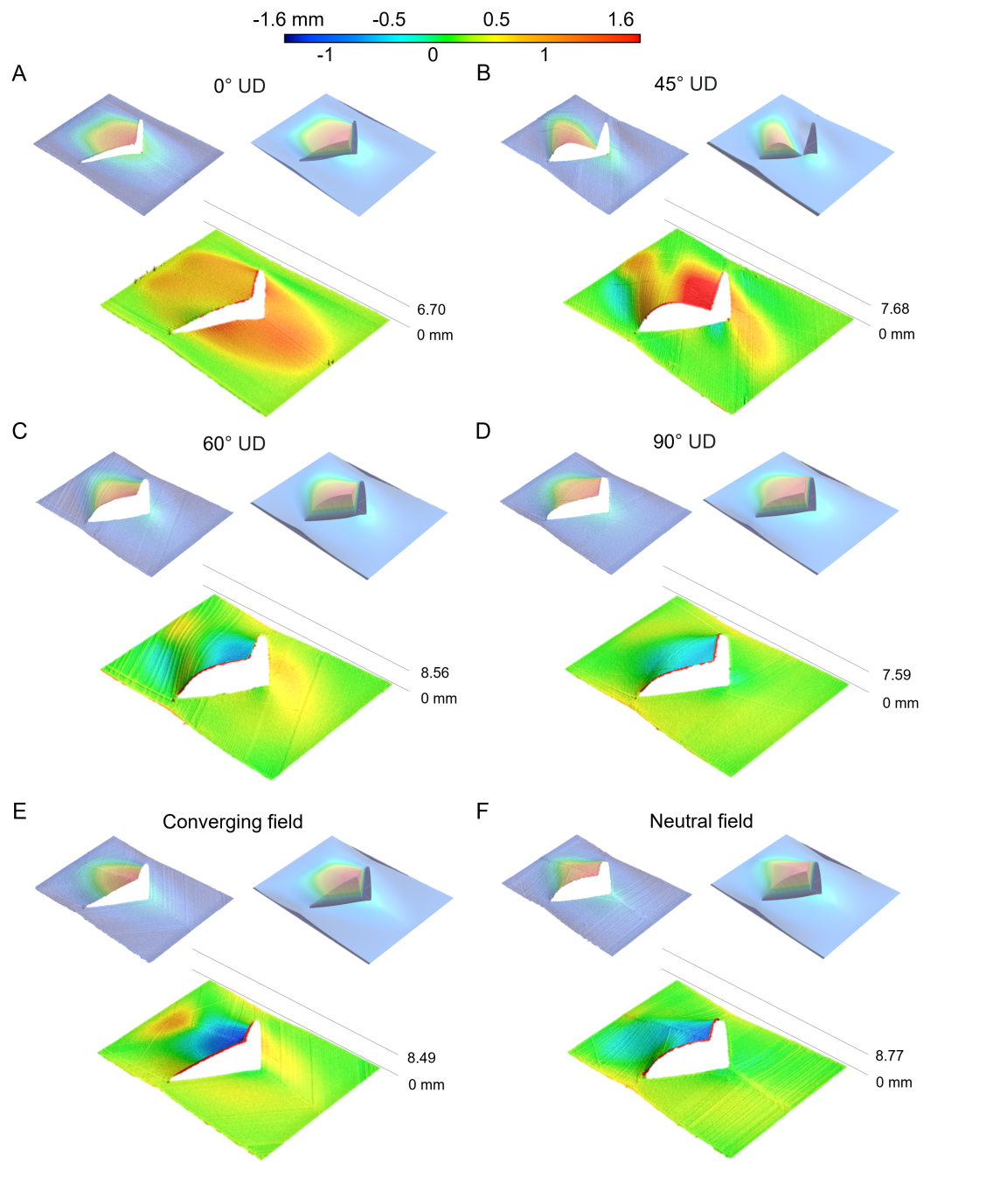

Figure 5.12: A: Comparison between 0 degrees UD material orientation FE results and actual test data at 1.5 mm displacement. B: Comparison between +45 degrees UD material orientation FE results and actual test data at 2.5 mm displacement. C: Comparison between +60 degrees UD material orientation FE results and actual test data at 2.5 mm displacement. D: Comparison between 90 degrees UD material orientation FE results and actual test data at 2.5 mm displacement. E: Comparison between converging material orientation field FE results and actual test data at 2.0 mm displacement. F: Comparison between neutral material orientation field FE results and actual test data at 3.0 mm displacement.

5.4.3. Generating new results

As the FE model is able to accurately capture the fibre steering effect in kirigami structures, it can be used to generate new results without the need for experimental data. This greatly reduces the time to analyse a particular buckled shape with its respective fibre pattern.

The geometry of the model is parameterized, therefore it can be used to create kirigami structures with multiple unit cells. As a first exploration of using the FE model to generate new results, the angled cut unit cell is diagonally patterned in a 2 by 2 grid as can be seen in 5.13A. This particular kirigami structure has 3 full sized leaves that will buckle out-of-plane. The structure is then divided into three areas as indicated by the dashed lines, each area contains a different material orientation (-45°, +45° or 0°). With this material orientation definition, both kirigami leaves that are located on the bottom row will point inward and the middle leaf on the top row will remain symmetric when stretched, as can be seen in 5.13B and 5.13C. The stretched state of the kirigami structure resembles the riblets that are located on the denticles of shark skin. The main aim of this simulation is to show that kirigami structures with a large amount of unit cells can be simulated in which deformation behaviour can be locally programmed by altering the fibre pattern. As previously discussed, this local geometry optimization is also seen in shark skin denticles.

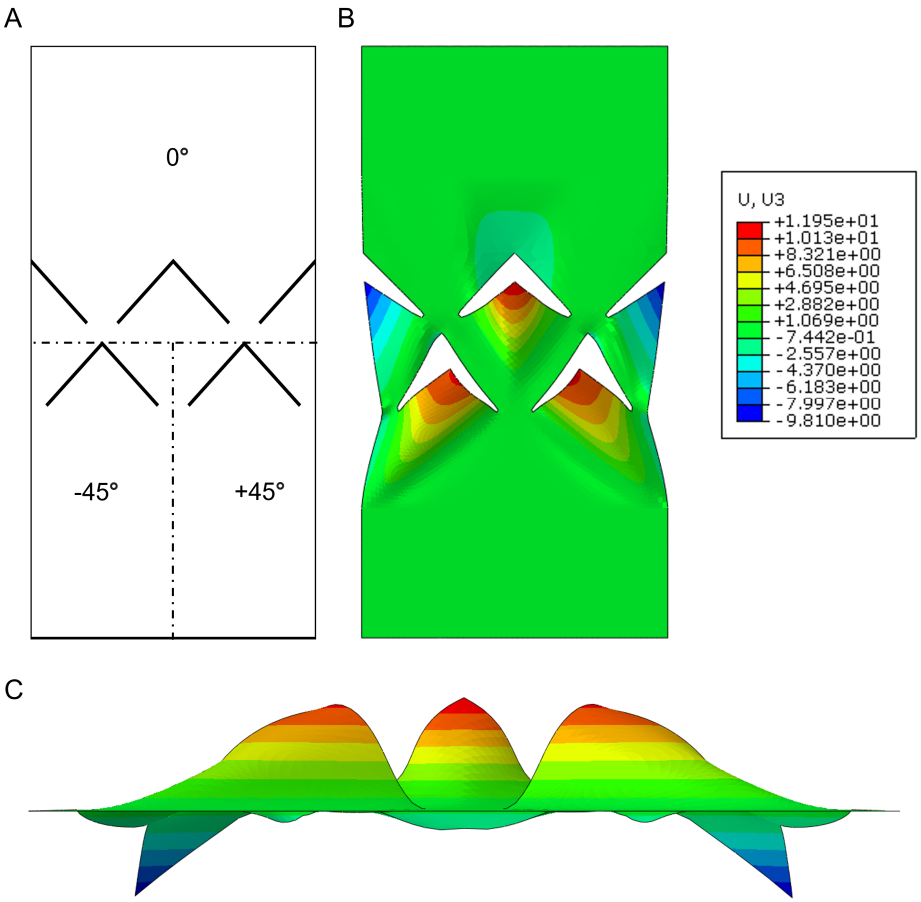

Figure 5.13: A: Angled cut unit cell is diagonally patterned in a 2 by 2 grid. The kirigami structure is divided in three regions with different fibre orientations such that the out-of-plane behaviour of each buckling surface is altered. B: Out-of-plane displacement of the kirigami structure at 4.5 mm in-plane displacement. The two kirigami leaves on the bottom row move inward, and the leaf in the middle on the top row moves out-of-plane symmetrically. C: Front view of the fibre steered kirigami structure to highlight shark skin riblet resemblance.

6

Conclusion

In this work, it was demonstrated that kirigami deformation behaviour can be controlled by tailoring the anisotropic material that is used to create the kirigami structure. The main goal was to find a relationship between the material pattern and the deformation behaviour of the kirigami structure. In order to reach this goal, fibre steered kirigami samples were manufactured and tested. A finite element (FE) model was made that is able to accurately predict the deformation behaviour of fibre steered kirigami. This model can drive future research, as analysis on the deformation behaviour is no longer solely dependent on experimental data.

In order to conclude this thesis, the research questions will be answered in this chapter. First of all, both sub-questions will be reintroduced and answered. Subsequently, the main research question will be answered.

1. **What is the relationship between the printed fibre pattern and the buckled shape of the kirigami structure under uniaxial loading?**

As kirigami will invert a global uniaxial stretch to a local compression of the kirigami leaf, the buckled shape of fibre steered angled cut kirigami can be predicted by following the thin plate buckling theory. Two rules are posed that are a direct result of this theory and can be used to estimate the shape of fibre steered kirigami, which are explained in figure 5.5. The first rule states that a sheet with clamped sides will buckle in the shape of a smooth, symmetric, parabola when subjected to compression. The second rule states that the local slope of the buckled parabola is directly proportional to the bending stiffness of the structure. As the bending stiffness is proportional to material stiffness, and the programmed kirigami exhibits variable stiffness, the slope of the parabola will change based on local material orientation. Two different shapes will follow by applying these rules. A shape will become more or less profound in the fibre steered kirigami structure based on the actual boundary conditions imposed by the surrounding material (kirigami hinge) that provides the compression. The stiffer this material is, the more towards a clamped boundary condition the material will behave, thereby the effect of material orientation is less profound. The buckled shape of the kirigami leaf will thereby approach a symmetric shape. When this material is less stiff, the material will impose a boundary condition that is weaker. The kirigami leaf will thereby buckle in a shape that follows its material orientation.

This theory was tested by analysing the buckled shapes of the variable UD fibre direction and symmetric orientation fields sample groups in subsections 5.2.4 and 5.2.5 respectively. As expected, the 0-, and 90 degree UD samples showed a symmetric buckled shape, the 90 degree UD sample showed a smaller out-of-plane deformation compared to the 0 degree UD sample. This could be expected, as the material in the direction of compression is stiffer for the 90 degree UD sample. All samples with an off-axis UD material orientation showed asymmetric out-of-plane behaviour. The shape skewed towards a direction in which it followed the least stiff direction, which was perpendicular to the UD fibre direction. The symmetric orientation field samples did not show significant differences between their respective shapes. It turns out that accurately predicting their buckled shapes is difficult by using basic

reasoning with thin plate buckling theory, as there are multiple fibre orientations present in the structure. However, a validated finite element model could be able to accurately predict these shapes.

2. **What are the characteristics of a validated finite element model that simulates the deformation of a kirigami structure with printed fibres?**

A finite element (FE) model has been made that was able to accurately predict the deformation behaviour of fibre steered kirigami, this model was made in Abaqus. The material model was defined as 'lamina'. With this definition, the model will take the anisotropic nature of the material into account. The local material orientation defined by an orientation field was assigned to the model mesh element centroids through repeated interpolation. The boundary conditions imposed on the kirigami structure were defined such that they would represent the experimental buckled shape test. Boundary conditions were defined on the bottom- and top clamp, these boundary conditions fully encastered the clamping surfaces. In the first step of the analysis, the buckling surfaces of the kirigami structure were displaced in an out-of-plane direction. This way it was ensured that the kirigami structure had a repeatable buckling direction during the tensile step (step 2 in the simulation) and that its respective buckled shape could be compared to experimental data. The FE model was validated by comparing the simulated kirigami tip deflection and kirigami shape to experimental data. Results show that the FE model is able to accurately predict the buckling behaviour of fibre steered kirigami as the relative error in maximum out-of-plane deformation did not exceed 13.7%. Furthermore, the buckled shapes that resulted from simulation approached the buckled shapes that followed from experimental data.

As the FE model is able to accurately capture the fibre steering effect in kirigami structures, it can be used to generate new results without the need for experimental data. This greatly reduces the time to analyse a particular buckled shape with its respective fibre pattern. The model can be used to simulate fibre steered kirigami structures with a large amount of unit cells. By locally changing material orientation, the deformation behaviour of a particular unit cell can be programmed (see subsection 5.4.3). This local geometry optimization is also seen in shark skin denticles.

The main research question posed in this thesis was:

- **How can the buckled shape of angled cut kirigami structures be controlled by exploiting the anisotropy that results from 3D-printed TPU CF material?**

The answer to this research question can be formulated by combining the answers of both sub-questions. This study showed that by tailoring the anisotropic TPU CF material in specific orientation fields, the deformation behaviour of kirigami can be altered. As the kirigami buckling surface is essentially a thin plate in compression, the classical plate buckling theory can be used to estimate the buckled shape of the kirigami structure. However, when multiple different fibre orientations are present in the kirigami structure it becomes less straightforward to estimate the buckled shape through logical reasoning because the stiffness of the material changes locally along the buckled parabolic cross-section. In order to accurately estimate these shapes, an FE model can be used. The FE model that is developed in this thesis is able to accurately predict the buckling behaviour of fibre steered kirigami. The model can be used to generate new results without the need for experimental data. An example of this can be seen in subsection 5.4.3, in which the FE model is used to simulate a kirigami structure with multiple unit cells and locally varying fibre direction. This structure resembles the riblets that are present on shark skin denticles. Furthermore, this simulation shows that a single unit cell in a larger kirigami structure can be programmed, as also seen in locally optimized shark skin.

7

Recommendations

Based on the findings in this study, a few improvements and recommendations for future work can be posed. First of all, the values for the in-plane- and transverse shear moduli (G_{12}, G_{13} and G_{23}) that served as input for the Abaqus model were approximated based on literature. The value for the in-plane shear modulus (G_{12}) could have been deduced by conducting a $\pm 45^{\circ}$ tensile test as described by ISO 14129. This way, the material model as defined in Abaqus that approximated the mechanical behaviour of the TPU CF material, would be closer to the actual behaviour of the material. Shearing effects are largest for samples with an off-axis material orientation. The FE results that followed for these samples would be more accurate with an updated in-plane shear modulus. In particular the retraction of the kirigami leaf tip in the 45° UD sample was overestimated by the FE model, as shown in figure 5.11.

This work investigated the effect of fibre steering in kirigami with a single cut. Ideally, a kirigami structure with multiple cuts should be manufactured and tested as such structures are used in actual applications. By doing this, an optimization of the flow separation delay device can be made as mentioned in chapter 1. By following the locally optimized denticle geometries as observed in shark skin, a fibre steered kirigami structure with locally varying out-of-plane deformation behaviour can be manufactured and tested for its drag reducing capabilities on an airfoil. This structure can have leaves with varying out-of-plane displacement by changing the stiffness in the direction of compression or change from a symmetric shape to asymmetric shape by changing (unidirectional) material orientation. When extending this work to kirigami with multiple unit cells, it must be noted that the neighbour-neighbour effect will become apparent (as discussed in subsection 2.1.2). Hereby, a certain programmed kirigami unit cell will influence its adjacent unit cells with its curvature. This effect must be taken into consideration during the design of the material orientation field.

As discussed in subsection 2.2.1, the buckling direction of kirigami leaves can be biased by locally varying the sheet thickness. This study did not investigate the effect of material orientation on the buckling direction of the kirigami leaves. This bias could potentially occur in large tessellated fibre steered kirigami structures in which the neighbour-neighbour effect becomes apparent. The out-of-plane deformation is more profound in a kirigami leaf in which the stiffness is relatively low. The curvature that this buckled leaf will impose on its adjacent (stiffer) unit cells might cause their leaves to buckle in the opposite direction. Whether this fibre orientation induced buckling direction bias exists could be investigated in future work.

The fibre steered kirigami samples were all manufactured with one layer. By adding multiple layers, one can add laminate coupling effects which can be used as a design feature. Kirigami essentially couples in-plane (stretch) deformation to out-of-plane deformation of the leaf. By adding layers that are orientated in such a way that in-plane - out-of-plane laminate coupling is induced, one is essentially adding an extra rule that the buckled shape has to follow. Thereby, unlocking more different buckled shapes.

In this work, a relationship between the fibre pattern and the buckled shape of the kirigami structure was found through basic reasoning for simple (UD) orientation fields and with the help of an FE model for more complex orientation fields. However, the inverse relationship would be much more valuable to an (aerodynamics) engineer. A certain flow condition will give a particular shape that leads to a desired flow control capability. Therefore, an engineer would like to know a certain fibre pattern that belongs to the desired buckled shape. This can potentially be done by training a machine learning algorithm with buckled shapes and accompanying fibre patterns. When sufficiently trained, it might be able to generate a fibre pattern based on buckled shape input.

References

[1] "Sharks: Streamlined swimmers – harvard museums of science & culture." (), [Online]. Available: https://hmsc.harvard.edu/online-exhibits/sharks/ (visited on 10/26/2023).

[2] U. G. K. Wegst, H. Bai, E. Saiz, A. P. Tomsia, and R. O. Ritchie, "Bioinspired structural materials," *Nature Materials*, vol. 14, no. 1, pp. 23–36, Jan. 2015, Number: 1 Publisher: Nature Publishing Group, ISSN: 1476-4660. DOI: 10.1038/nmat4089. [Online]. Available: https://www.nature.com/articles/nmat4089 (visited on 10/03/2022).

[3] D. W. Bechert, M. Bartenwerfer, G. Hoppe, and W. .-. Reif, "Drag reduction mechanisms derived from shark skin," vol. 2, pp. 1044–1068, Jan. 1, 1986, Conference Name: IN: ICAS ADS Bibcode: 1986icas....2.1044B. [Online]. Available: https://ui.adsabs.harvard.edu/abs/1986icas...2.1044B (visited on 10/17/2023).

[4] P. Motta, M. L. Habegger, A. Lang, R. Hueter, and J. Davis, "Scale morphology and flexibility in the shortfin mako isurus oxyrinchus and the blacktip shark carcharhinus limbatus," *Journal of Morphology*, vol. 273, no. 10, pp. 1096–1110, 2012, _eprint: https://onlinelibrary.wiley.com/doi/pdf/10.1002/jmor.20047, ISSN: 1097-4687. DOI: 10.1002/jmor.20047. [Online]. Available: http://onlinelibrary.wiley.com/doi/abs/10.1002/jmor.20047 (visited on 10/17/2023).

[5] A. W. Lang *et al.*, "Movable shark scales act as a passive dynamic micro-roughness to control flow separation," *Bioinspiration & Biomimetics*, vol. 9, no. 3, p. 036 017, Jul. 2014, Publisher: IOP Publishing, ISSN: 1748-3190. DOI: 10.1088/1748-3182/9/3/036017. [Online]. Available: https://dx.doi.org/10.1088/1748-3182/9/3/036017 (visited on 10/17/2023).

[6] H. Ritchie and M. Roser, "Climate change and flying: What share of global CO2 emissions come from aviation?" *Our World in Data*, Sep. 27, 2023. [Online]. Available: https://ourworldindata.org/co2-emissions-from-aviation (visited on 10/17/2023).

[7] L. Gamble, A. Lamoureux, and M. Shtein, "Multifunctional composite kirigami skins for aerodynamic control," *Applied Physics Letters*, vol. 117, no. 25, p. 254 105, Dec. 21, 2020, Publisher: American Institute of Physics, ISSN: 0003-6951. DOI: 10.1063/5.0024501. [Online]. Available: https://aip.scitation.org/doi/full/10.1063/5.0024501 (visited on 01/31/2023).

[8] Y. Sun, W. Ye, Y. Chen, W. Fan, J. Feng, and P. Sareh, "Geometric design classification of kirigami-inspired metastructures and metamaterials," *Structures*, vol. 33, pp. 3633–3643, Oct. 1, 2021, ISSN: 2352-0124. DOI: 10.1016/j.istruc.2021.06.072. [Online]. Available: https://www.sciencedirect.com/science/article/pii/S2352012421005774 (visited on 01/31/2023).

[9] Y. Cho *et al.*, "Engineering the shape and structure of materials by fractal cut," *Proceedings of the National Academy of Sciences*, vol. 111, no. 49, pp. 17 390–17 395, Dec. 9, 2014, Publisher: Proceedings of the National Academy of Sciences. DOI: 10.1073/pnas.1417276111. [Online]. Available: https://www.pnas.org/doi/full/10.1073/pnas.1417276111 (visited on 02/02/2023).

[10] Y. Tang and J. Yin, "Design of cut unit geometry in hierarchical kirigami-based auxetic metamaterials for high stretchability and compressibility," *Extreme Mechanics Letters*, Frontiers in Mechanical Metamaterials, vol. 12, pp. 77–85, Apr. 1, 2017, ISSN: 2352-4316. DOI: 10.1016/j.eml.2016.07.005. [Online]. Available: https://www.sciencedirect.com/science/article/pii/S235243161630058X (visited on 02/02/2023).

[11] S. Shan, S. H. Kang, Z. Zhao, L. Fang, and K. Bertoldi, "Design of planar isotropic negative poisson's ratio structures," *Extreme Mechanics Letters*, vol. 4, pp. 96–102, Sep. 1, 2015, ISSN: 2352-4316. DOI: 10.1016/j.eml.2015.05.002. [Online]. Available: https://www.sciencedirect.com/science/article/pii/S2352431615000759 (visited on 02/02/2023).

[12] G. P. T. Choi, L. H. Dudte, and L. Mahadevan, "Programming shape using kirigami tessellations," *Nature Materials*, vol. 18, no. 9, pp. 999–1004, Sep. 2019, Number: 9 Publisher: Nature

Publishing Group, ISSN: 1476-4660. DOI: 10.1038/s41563-019-0452-y. [Online]. Available: https://www.nature.com/articles/s41563-019-0452-y (visited on 02/02/2023).

[13] A. Rafsanjani and K. Bertoldi, "Buckling-induced kirigami," *Physical Review Letters*, vol. 118, no. 8, p. 084 301, Feb. 21, 2017, Publisher: American Physical Society. DOI: 10.1103/PhysRevLett.118.084301. [Online]. Available: https://link.aps.org/doi/10.1103/PhysRevLett.118.084301 (visited on 02/01/2023).

[14] J. Tao, H. Khosravi, V. Deshpande, and S. Li, "Engineering by cuts: How kirigami principle enables unique mechanical properties and functionalities," *Advanced Science*, vol. n/a, p. 2 204 733, n/a, _eprint: https://onlinelibrary.wiley.com/doi/pdf/10.1002/advs.202204733, ISSN: 2198-3844. DOI: 10.1002/advs.202204733. [Online]. Available: https://onlinelibrary.wiley.com/doi/abs/10.1002/advs.202204733 (visited on 12/30/2022).

[15] M. Isobe and K. Okumura, "Initial rigid response and softening transition of highly stretchable kirigami sheet materials," *Scientific Reports*, vol. 6, no. 1, p. 24 758, Apr. 27, 2016, Number: 1 Publisher: Nature Publishing Group, ISSN: 2045-2322. DOI: 10.1038/srep24758. [Online]. Available: https://www.nature.com/articles/srep24758 (visited on 01/05/2023).

[16] A. T. Zehnder and Y. K. Potdar, "Williams meets von karman: Mode coupling and nonlinearity in the fracture of thin plates," *International Journal of Fracture*, vol. 93, no. 1, pp. 409–429, Sep. 1, 1998, ISSN: 1573-2673. DOI: 10.1023/A:1007512716475. [Online]. Available: https://doi.org/10.1023/A:1007512716475 (visited on 02/27/2023).

[17] R. Brighenti, "Buckling of cracked thin-plates under tension or compression," *Thin-Walled Structures*, vol. 43, pp. 209–224, Feb. 1, 2005. DOI: 10.1016/j.tws.2004.07.006.

[18] Y. Tang, G. Lin, S. Yang, Y. K. Yi, R. D. Kamien, and J. Yin, "Programmable kiri-kirigami metamaterials," *Advanced Materials*, vol. 29, no. 10, p. 1 604 262, 2017, _eprint: https://onlinelibrary.wiley.com/doi/pdf/10.1002/adma.201604262, ISSN: 1521-4095. DOI: 10.1002/adma.201604262. [Online]. Available: https://onlinelibrary.wiley.com/doi/abs/10.1002/adma.201604262 (visited on 03/03/2023).

[19] M. A. Dias *et al.*, "Kirigami actuators," *Soft Matter*, vol. 13, no. 48, pp. 9087–9092, Dec. 13, 2017, Publisher: The Royal Society of Chemistry, ISSN: 1744-6848. DOI: 10.1039/C7SM01693J. [Online]. Available: https://pubs.rsc.org/en/content/articlelanding/2017/sm/c7sm01693j (visited on 02/27/2023).

[20] Y. Yang, M. A. Dias, and D. P. Holmes, "Multistable kirigami for tunable architected materials," *Physical Review Materials*, vol. 2, no. 11, p. 110 601, Nov. 20, 2018, Publisher: American Physical Society. DOI: 10.1103/PhysRevMaterials.2.110601. [Online]. Available: https://link.aps.org/doi/10.1103/PhysRevMaterials.2.110601 (visited on 02/27/2023).

[21] T. C. Shyu *et al.*, "A kirigami approach to engineering elasticity in nanocomposites through patterned defects," *Nature Materials*, vol. 14, no. 8, pp. 785–789, Aug. 2015, Number: 8 Publisher: Nature Publishing Group, ISSN: 1476-4660. DOI: 10.1038/nmat4327. [Online]. Available: https://www.nature.com/articles/nmat4327 (visited on 02/10/2023).

[22] A. Lamoureux, K. Lee, M. Shlian, S. R. Forrest, and M. Shtein, "Dynamic kirigami structures for integrated solar tracking," *Nature Communications*, vol. 6, no. 1, p. 8092, Sep. 8, 2015, Number: 1 Publisher: Nature Publishing Group, ISSN: 2041-1723. DOI: 10.1038/ncomms9092. [Online]. Available: https://www.nature.com/articles/ncomms9092 (visited on 03/07/2023).

[23] A. Rafsanjani, L. Jin, B. Deng, and K. Bertoldi, "Propagation of pop ups in kirigami shells," *Proceedings of the National Academy of Sciences*, vol. 116, no. 17, pp. 8200–8205, Apr. 23, 2019, Publisher: Proceedings of the National Academy of Sciences. DOI: 10.1073/pnas.1817763116. [Online]. Available: https://www.pnas.org/doi/10.1073/pnas.1817763116 (visited on 03/03/2023).

[24] T. A. Osswald, J. Puentes, and J. Kattinger, "Fused filament fabrication melting model," *Additive Manufacturing*, vol. 22, pp. 51–59, Aug. 1, 2018, ISSN: 2214-8604. DOI: 10.1016/j.addma.2018.04.030. [Online]. Available: https://www.sciencedirect.com/science/article/pii/S221486041730458X (visited on 10/27/2022).

[25] B. Shaqour *et al.*, "Gaining a better understanding of the extrusion process in fused filament fabrication 3d printing: A review," *The International Journal of Advanced Manufacturing Technology*,

vol. 114, no. 5, pp. 1279–1291, May 1, 2021, ISSN: 1433-3015. DOI: 10.1007/s00170-021-06918-6. [Online]. Available: https://doi.org/10.1007/s00170-021-06918-6 (visited on 10/19/2022).

[26] A. Dey, I. N. Roan Eagle, and N. Yodo, "A review on filament materials for fused filament fabrication," *Journal of Manufacturing and Materials Processing*, vol. 5, no. 3, p. 69, Sep. 2021, Number: 3 Publisher: Multidisciplinary Digital Publishing Institute, ISSN: 2504-4494. DOI: 10.3390/jmmp5030069. [Online]. Available: https://www.mdpi.com/2504-4494/5/3/69 (visited on 10/19/2022).

[27] W. C. Smith and R. W. Dean, "Structural characteristics of fused deposition modeling polycarbonate material," *Polymer Testing*, vol. 32, no. 8, pp. 1306–1312, Dec. 1, 2013, ISSN: 0142-9418. DOI: 10.1016/j.polymertesting.2013.07.014. [Online]. Available: https://www.sciencedirect.com/science/article/pii/S0142941813001463 (visited on 02/15/2023).

[28] A. Dorigato, V. Moretti, S. Dul, S. H. Unterberger, and A. Pegoretti, "Electrically conductive nanocomposites for fused deposition modelling," *Synthetic Metals*, vol. 226, pp. 7–14, Apr. 1, 2017, ISSN: 0379-6779. DOI: 10.1016/j.synthmet.2017.01.009. [Online]. Available: https://www.sciencedirect.com/science/article/pii/S0379677917300097 (visited on 02/15/2023).

[29] J. M. Chacón, M. A. Caminero, E. García-Plaza, and P. J. Núñez, "Additive manufacturing of PLA structures using fused deposition modelling: Effect of process parameters on mechanical properties and their optimal selection," *Materials & Design*, vol. 124, pp. 143–157, Jun. 15, 2017, ISSN: 0264-1275. DOI: 10.1016/j.matdes.2017.03.065. [Online]. Available: https://www.sciencedirect.com/science/article/pii/S0264127517303143 (visited on 02/15/2023).

[30] S. F. Costa, F. M. Duarte, and J. A. Covas, "Estimation of filament temperature and adhesion development in fused deposition techniques," *Journal of Materials Processing Technology*, vol. 245, pp. 167–179, Jul. 1, 2017, ISSN: 0924-0136. DOI: 10.1016/j.jmatprotec.2017.02.026. [Online]. Available: https://www.sciencedirect.com/science/article/pii/S0924013617300791 (visited on 02/15/2023).

[31] N. Aliheidari, R. Tripuraneni, A. Ameli, and S. Nadimpalli, "Fracture resistance measurement of fused deposition modeling 3d printed polymers," *Polymer Testing*, vol. 60, pp. 94–101, Jul. 1, 2017, ISSN: 0142-9418. DOI: 10.1016/j.polymertesting.2017.03.016. [Online]. Available: https://www.sciencedirect.com/science/article/pii/S0142941817300065 (visited on 02/15/2023).

[32] D. Drummer, S. Cifuentes□Cuéllar, and D. Rietzel, "Suitability of PLA/TCP for fused deposition modeling," *Rapid Prototyping Journal*, vol. 18, no. 6, pp. 500–507, Jan. 1, 2012, Publisher: Emerald Group Publishing Limited, ISSN: 1355-2546. DOI: 10.1108/13552541211272045. [Online]. Available: https://doi.org/10.1108/13552541211272045 (visited on 02/15/2023).

[33] H. Li, T. Wang, J. Sun, and Z. Yu, "The effect of process parameters in fused deposition modelling on bonding degree and mechanical properties," *Rapid Prototyping Journal*, vol. 24, no. 1, pp. 80–92, Jan. 1, 2018, Publisher: Emerald Publishing Limited, ISSN: 1355-2546. DOI: 10.1108/RPJ-06-2016-0090. [Online]. Available: https://doi.org/10.1108/RPJ-06-2016-0090 (visited on 02/15/2023).

[34] A. Alafaghani and A. Qattawi, "Investigating the effect of fused deposition modeling processing parameters using taguchi design of experiment method," *Journal of Manufacturing Processes*, vol. 36, pp. 164–174, Dec. 1, 2018, ISSN: 1526-6125. DOI: 10.1016/j.jmapro.2018.09.025. [Online]. Available: https://www.sciencedirect.com/science/article/pii/S1526612518314026 (visited on 02/15/2023).

[35] S. Xiaoyong, C. Liangcheng, M. Honglin, G. Peng, B. Zhanwei, and L. Cheng, "Experimental analysis of high temperature PEEK materials on 3d printing test," in *2017 9th International Conference on Measuring Technology and Mechatronics Automation (ICMTMA)*, ISSN: 2157-1481, Jan. 2017, pp. 13–16. DOI: 10.1109/ICMTMA.2017.0012.

[36] J. Torres, M. Cole, A. Owji, Z. DeMastry, and A. Gordon, "An approach for mechanical property optimization of fused deposition modeling with polylactic acid via design of experiments," *Rapid Prototyping Journal*, vol. 22, no. 2, pp. 387–404, 2016, ISSN: 1355-2546. DOI: 10.1108/RPJ-07-2014-0083.

[37] F. Ning, W. Cong, Y. Hu, and H. Wang, "Additive manufacturing of carbon fiber-reinforced plastic composites using fused deposition modeling: Effects of process parameters on tensile properties," *Journal of Composite Materials*, vol. 51, no. 4, pp. 451–462, Feb. 1, 2017, Publisher: SAGE Publications Ltd STM, ISSN: 0021-9983. DOI: 10.1177/0021998316646169. [Online]. Available: https://doi.org/10.1177/0021998316646169 (visited on 02/15/2023).

[38] M. Vaezi and C. K. Chua, "Effects of layer thickness and binder saturation level parameters on 3d printing process," *The International Journal of Advanced Manufacturing Technology*, vol. 53, no. 1, pp. 275–284, Mar. 1, 2011, ISSN: 1433-3015. DOI: 10.1007/s00170-010-2821-1. [Online]. Available: https://doi.org/10.1007/s00170-010-2821-1 (visited on 02/15/2023).

[39] A. K. Sood, R. K. Ohdar, and S. S. Mahapatra, "Parametric appraisal of fused deposition modelling process using the grey taguchi method," *Proceedings of the Institution of Mechanical Engineers, Part B: Journal of Engineering Manufacture*, vol. 224, no. 1, pp. 135–145, Jan. 1, 2010, Publisher: IMECHE, ISSN: 0954-4054. DOI: 10.1243/09544054JEM1565. [Online]. Available: https://doi.org/10.1243/09544054JEM1565 (visited on 02/15/2023).

[40] A. Garg and A. Bhattacharya, "An insight to the failure of FDM parts under tensile loading: Finite element analysis and experimental study," *International Journal of Mechanical Sciences*, vol. 120, pp. 225–236, Jan. 1, 2017, ISSN: 0020-7403. DOI: 10.1016/j.ijmecsci.2016.11.032. [Online]. Available: https://www.sciencedirect.com/science/article/pii/S0020740316309596 (visited on 02/15/2023).

[41] G. W. Melenka, J. S. Schofield, M. R. Dawson, and J. P. Carey, "Evaluation of dimensional accuracy and material properties of the MakerBot 3d desktop printer," *Rapid Prototyping Journal*, vol. 21, no. 5, D. Eujin Pei, Ed., pp. 618–627, Jan. 1, 2015, Publisher: Emerald Group Publishing Limited, ISSN: 1355-2546. DOI: 10.1108/RPJ-09-2013-0093. [Online]. Available: https://doi.org/10.1108/RPJ-09-2013-0093 (visited on 02/15/2023).

[42] S.-H. Ahn, M. Montero, D. Odell, S. Roundy, and P. K. Wright, "Anisotropic material properties of fused deposition modeling ABS," *Rapid Prototyping Journal*, vol. 8, no. 4, pp. 248–257, Jan. 1, 2002, Publisher: MCB UP Ltd, ISSN: 1355-2546. DOI: 10.1108/13552540210441166. [Online]. Available: https://doi.org/10.1108/13552540210441166 (visited on 02/15/2023).

[43] J. Nakajima, K. Fayazbakhsh, and Y. Teshima, "Experimental study on tensile properties of 3d printed flexible kirigami specimens," *Additive Manufacturing*, vol. 32, p. 101 100, Mar. 1, 2020, ISSN: 2214-8604. DOI: 10.1016/j.addma.2020.101100. [Online]. Available: https://www.sciencedirect.com/science/article/pii/S2214860419320123 (visited on 02/09/2023).

[44] S. Amin, "Additive manufacturing of kirigami metasurfaces," 2022. [Online]. Available: https://repository.tudelft.nl/islandora/object/uuid%3Ac6bfe155-e126-48eb-9c5c-c5115d05494f (visited on 02/27/2023).

[45] R. I. Tanner, "A theory of die-swell," *Journal of Polymer Science Part A-2: Polymer Physics*, vol. 8, no. 12, pp. 2067–2078, 1970, _eprint: https://onlinelibrary.wiley.com/doi/pdf/10.1002/pol.1970.160081203, ISSN: 1542-9377. DOI: 10.1002/pol.1970.160081203. [Online]. Available: http://onlinelibrary.wiley.com/doi/abs/10.1002/pol.1970.160081203 (visited on 10/16/2023).

[46] B. P. Heller, D. E. Smith, and D. A. Jack, "Effects of extrudate swell and nozzle geometry on fiber orientation in fused filament fabrication nozzle flow," *Additive Manufacturing*, Special Issue on Modeling & Simulation for Additive Manufacturing, vol. 12, pp. 252–264, Oct. 1, 2016, ISSN: 2214-8604. DOI: 10.1016/j.addma.2016.06.005. [Online]. Available: https://www.sciencedirect.com/science/article/pii/S2214860416301166 (visited on 03/17/2023).

[47] E. Bertevas, J. Férec, B. C. Khoo, G. Ausias, and N. Phan-Thien, "Smoothed particle hydrodynamics (SPH) modeling of fiber orientation in a 3d printing process," *Physics of Fluids*, vol. 30, no. 10, p. 103 103, Oct. 2018, Publisher: American Institute of Physics, ISSN: 1070-6631. DOI: 10.1063/1.5047088. [Online]. Available: https://aip.scitation.org/doi/full/10.1063/1.5047088 (visited on 03/17/2023).

[48] "3d printer filaments / pla filaments,ABS,hips," Smart Materials 3D. (), [Online]. Available: https://www.smartmaterials3d.com/en/ (visited on 10/25/2023).

[49] C. Houriet, V. Damodaran, K. Masania, C. Mascolo, S. Gantenbein, and D. Peeters. “ShapingMatterLab / slith3r · GitLab,” Submitted. (), [Online]. Available: https://gitlab.tudelft.nl/shapingmatterlab/slith3r (visited on 10/25/2023).

[50] S. N. Grebenyuk, “The shear modulus of a composite material with a transversely isotropic matrix and a fibre,” *Journal of Applied Mathematics and Mechanics*, vol. 78, no. 2, pp. 187–191, Jan. 1, 2014, ISSN: 0021-8928. DOI: 10.1016/j.jappmathmech.2014.07.012. [Online]. Available: https://www.sciencedirect.com/science/article/pii/S0021892814000690 (visited on 10/26/2023).

[51] M. Tausif, A. Pliakas, T. O’Haire, P. Goswami, and S. J. Russell, “Mechanical properties of non-woven reinforced thermoplastic polyurethane composites,” *Materials*, vol. 10, no. 6, p. 618, Jun. 2017, Number: 6 Publisher: Multidisciplinary Digital Publishing Institute, ISSN: 1996-1944. DOI: 10.3390/ma10060618. [Online]. Available: https://www.mdpi.com/1996-1944/10/6/618 (visited on 10/26/2023).

[52] N. Pan, “The elastic constants of randomly oriented fiber composites: A new approach to prediction,” *Science and Engineering of Composite Materials*, vol. 5, no. 2, pp. 63–72, Jun. 1, 1996, Publisher: De Gruyter, ISSN: 2191-0359. DOI: 10.1515/SECM.1996.5.2.63. [Online]. Available: http://www.degruyter.com/document/doi/10.1515/SECM.1996.5.2.63/html (visited on 10/26/2023).

A

Mesh Convergence Study

The simulated buckled shapes of the kirigami surfaces that belong to the data points in figure 4.15, can be seen in figure A.1. The shape of the 45 degrees cut angle, 0.2 δ/L ratio, +45 degree UD material orientation sample converges after 1844 elements which corresponds to an average mesh size of 1.57 mm. In order to properly show the buckled shapes, the mesh was not rendered.

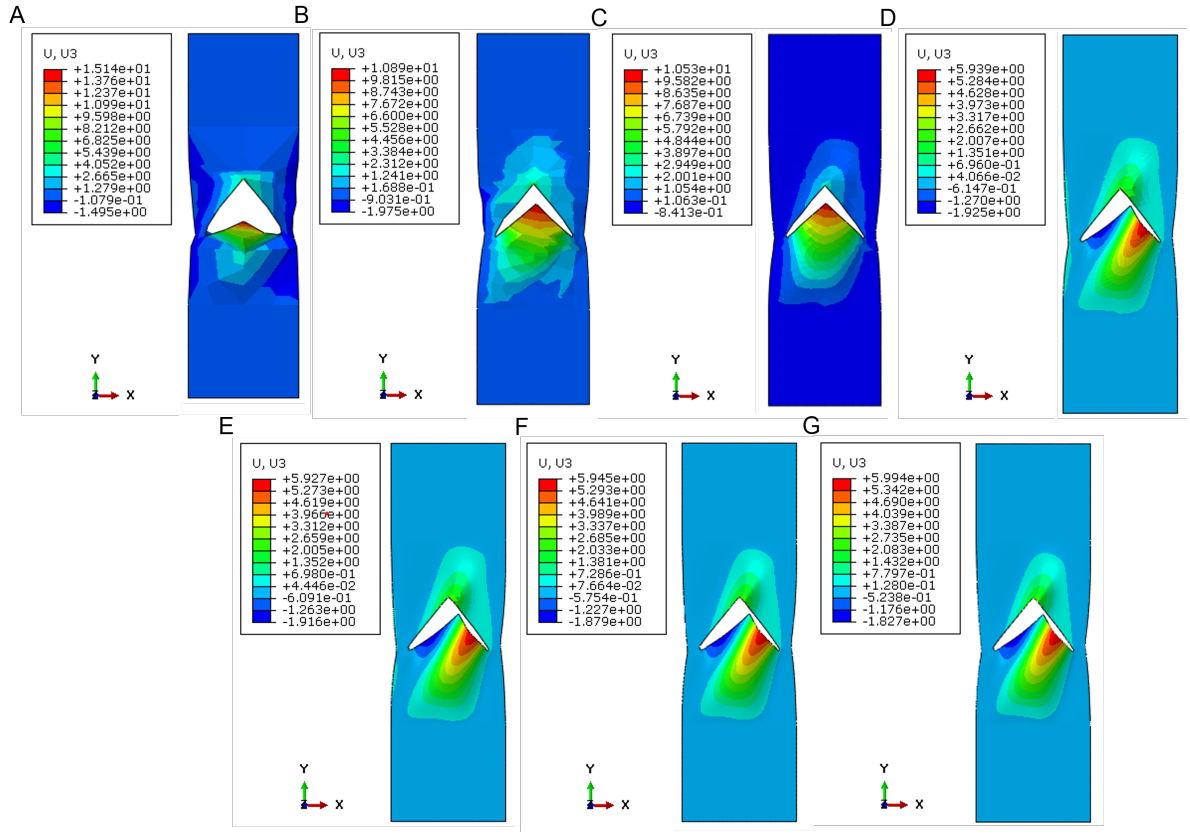

Figure A.1: A: Simulated shape of sample with an average mesh size of 12.5 mm, corresponding to a total of 55 elements. B: Simulated shape of sample with an average mesh size of 6.25 mm, corresponding to a total of 150 elements. C: Simulated shape of sample with an average mesh size of 3.125 mm, corresponding to a total of 528 elements. D: Simulated shape of sample with an average mesh size of 1.563 mm, corresponding to a total of 1844 elements. E: Simulated shape of sample with an average mesh size of 0.781 mm, corresponding to a total of 7747 elements. F: Simulated shape of sample with an average mesh size of 0.391 mm, corresponding to a total of 31274 elements. G: Simulated shape of sample with an average mesh size of 0.195 mm, corresponding to a total of 125895 elements.

B

Deviation in identical sample measurements

All buckled shape tests performed had an identical sample count of 2, which is small for a quantitative study. This study investigates the limits and opportunities that fibre steering in kirigami brings. Therefore, the exploration of the different shapes that resulted from various fibre patterns was valued more than a lower standard deviation in the results. In order to show that the measurements which have been used for analysis do have quantitative meaning, a surface comparison study is done to highlight the differences between identical sample measurements. This comparison study is performed by using the exact same approach as in the FE- and experimental shape comparison as shown in figure 5.12.

In order to have a relatively low effect of the pre-stress introduced during clamping of the samples, while simultaneously ensuring that there is no plastic deformation, shape measurements in the middle of a stretch cycle of a sample were used. The ultimate displacement was not always equal between identical samples. Therefore, measurements at the lowest displacement value were used to compare both shapes. The Keyence VR-5000 software is used to overlap both shapes. As the shapes compare rather well, the software is able to overlap the surfaces automatically. The resulting geometry is the 3D surface of sample 1, on which the differences with respect to the 3D surface of sample 2 are projected. The resulting surfaces of 5 samples across multiple sample groups can be seen in figure B.1. The scale, indicating the values of the differences between the identical samples has been normalized. In order to quantify how well the surfaces compare, the relative difference in the out-of-plane displacement between both samples (error) is calculated. The results are indicated in table B.1. The comparison study has been done for every sample. However, the table and figure only show the results of five samples with the largest error. The error was lower than 7.78% for every sample.

Table B.1: Data corresponding to the surface comparison study

Sample	Displace-ment (mm)	Out-of-plane displacement sample 1 (mm)	Out-of-plane displacement sample 2 (mm)	Largest local difference (mm)	Error (%)	Figure
Cut angle 60 degrees, +45 degrees UD	2.0	6.95	6.94	0.20	0.14	B.1A
Converging field	2.0	7.87	7.94	-0.63	0.88	B.1B
δ/L 0.138, +45 degrees UD	2.0	8.99	9.03	0.54	0.44	B.1C
+30 degrees UD	2.0	6.76	7.33	0.67	7.78	B.1D
90 degrees UD	2.5	6.86	6.89	-0.572	0.44	B.1E

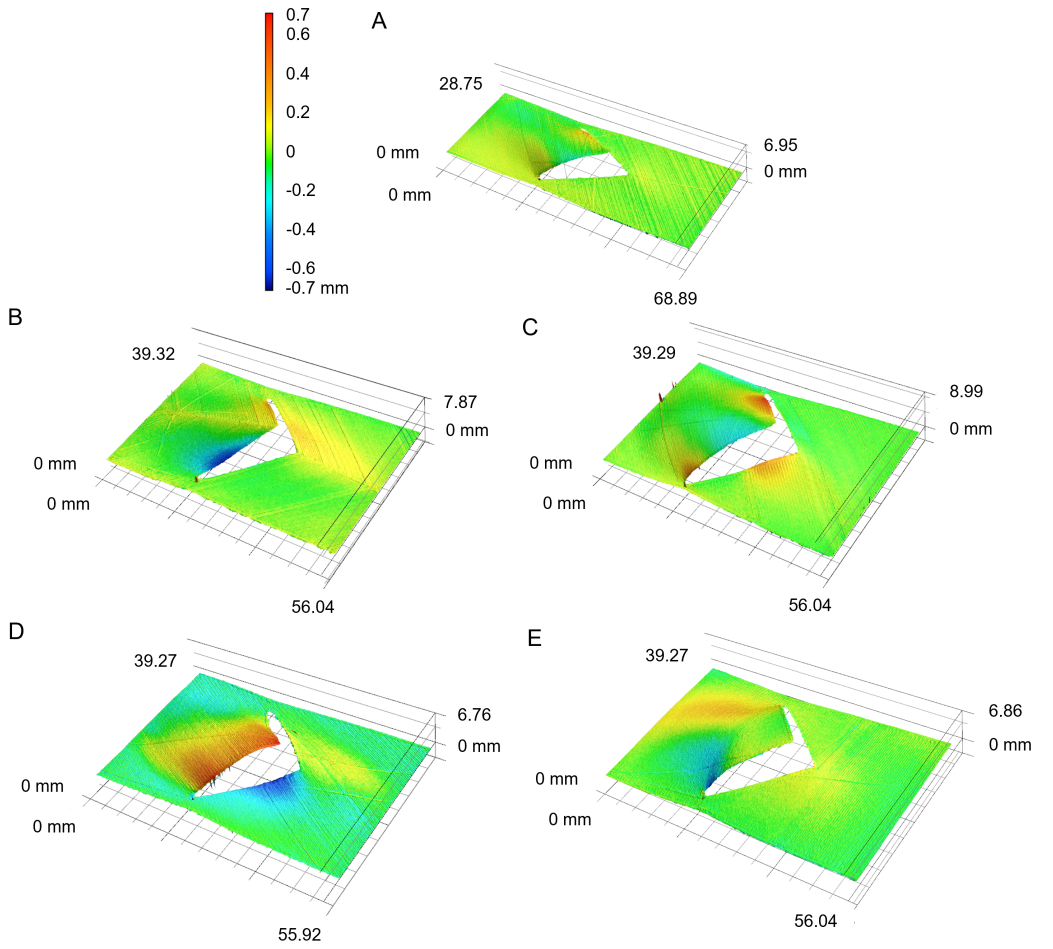

Figure B.1: A: Comparison of identical cut angle 60 degrees, +45 degrees UD samples at 2.0 mm displacement. B: Comparison of identical converging field samples at 2.0 mm displacement. C: Comparison of identical δ/L 0.138, +45 degrees UD samples at 2.0 mm displacement. D: Comparison of identical +30 degrees UD samples at 2.0 mm displacement. E: Comparison of identical 90 degrees UD samples at 2.5 mm displacement.